

Searching For Planets During Predicted Mesolensing Events

Masters Thesis

James Matthews
School of Physics and Astronomy
University of Southampton

Project Supervisor: Dr Rosanne Di Stefano

May 4, 2012

Abstract

Gravitational microlensing has detected 15 exoplanets. Thus far, exoplanet lensing searches have relied on passive monitoring, in which a field is regularly observed in anticipation of photometric variability which could signal a serendipitous lensing event. Here we focus on lensing with two main distinguishing features. First, we consider nearby lenses ($d \lesssim 500$ pc), or mesolenses. Mesolenses generally have larger Einstein angles and higher proper motions than those further away. Both of these properties result in a higher frequency of events, which is why mesolensing is referred to as a ‘high-probability’ subset of microlensing. Second, we assess the prospects for discovering planets during mesolensing events which can be predicted in advance. We have studied lenses with planet orbital separations both larger and smaller than the Einstein radius, and we have shown that this method can detect planets in a wide range of orbits. In particular, we have studied the VB 10 event originally predicted by Lépine & Di Stefano (2012) in detail, and conducted simulations of the possible approaches. This event has been used as a specific case study for the general class of high proper motion lenses that can be used as an effective probe for planetary companions. As an example of the procedure for predicting further events, we have studied the mesolensing event rate in the Kepler field. We estimate rates of detectable events between high proper motion stars (from the SUPERBLINK lists) and stars in the 2MASS, Pan-STARRS 3π and USNO A2.0 catalogues at 0.03, 0.24 and 0.06 per year respectively. We also present the prediction of a lensing event involving the nearby star GJ1214, with a distance of closest approach of $b = 446 \pm 161$ mas and a date of closest approach of 23 July 2025 (± 62.1 days). We identify procedures to image the corresponding regions and constrain the uncertainties for each predicted event, and have carried out this process for GJ1214. Plans to design a multi-waveband observing program to monitor predicted mesolensing events have been outlined, and implemented in the early stages of the ‘PLAN-IT’ program.

Contents

List of Figures	3
1 Introduction	4
1.1 Exoplanets	4
1.2 Gravitational Lensing and Microlensing	6
1.3 Principal Objectives	7
2 Theoretical Background	8
2.1 Lensing Theory	8
2.2 Mesolensing	10
2.3 Detecting Planets	11
2.3.1 Other Types of Planet-Lens Signatures	11
2.3.2 Inclination and Eccentricity: Orbital Elements and Their Effect on Lensing	13
3 The VB 10 Predicted Mesolensing Event	15
3.1 A Prediction, its Implications, and Challenges	15
3.1.1 Observational Difficulties	18
3.2 Does VB 10 Have Planets?	19
3.3 Method: Computer Simulations	20
3.4 Three Orbital Regimes	21
3.4.1 The Wide Orbit Regime	21
3.4.2 The Close Orbit Regime	26
3.4.3 The Resonant Regime	27
3.5 Results from Simulations	27
3.5.1 Detection of Reflex Motion	31
3.5.2 The Effects of Orbital Orientation	31
3.6 Observations, Prospects and Future Work on the VB 10 Event	33
4 Predicting Future Events	36
4.1 Method and Catalogues	36

4.2	Lensing in the Kepler Field	38
4.2.1	Why Kepler?	38
4.2.2	The Mesolensing Event Rate	39
4.3	2MASS Predictions	41
4.3.1	GJ1214	41
4.4	Overall Prospects and Future Work	43
5	Conclusion	45
	Acknowledgements	47
	Bibliography	48
A	VB 10 Simulation Code	55
B	Wide-Orbit Planets	62
C	Catalogue of VB 10 Simulation Results for Selected Approaches	65

List of Figures

1.1	Known exoplanets	5
2.1	Geometry of a point-mass lens	8
2.2	Light curve for OGLE-2006-BLG-109L	12
2.3	The geometrical quantities defining an orbit	14
3.1	<i>HST</i> and MEarth images of VB 10	16
3.2	Possible times of closest approach for the VB 10 event	17
3.3	Possible VB 10 approaches, and orbital regimes	17
3.4	Solar angle for VB 10 over time	19
3.5	Example wide, close and resonant light curves	22
3.6	Isomagnification contours around VB 10 for two different wide orbits	23
3.7	The size of the region of deviation for $\delta = 0.1, 0.25, 0.625$	25
3.8	VB 10 simulated results showing possible planetary events	28
3.9	VB 10 caustic crossing statistics	29
3.10	Planet detection probabilities during the VB 10 event	30
3.11	The maximum magnification difference from reflex motion	32
3.12	The effect of orientation for $\alpha = 5, \beta = 3$	33
3.13	VB 10 light curve from USNO and MEarth observations	35
4.1	Kepler field of view	39
4.2	Event rates with catalogues in the <i>Kepler</i> field	40
4.3	<i>HST</i> image of the field around GJ1214.	43
VB 10 Simulation Results:		65
C.1	Clockwise, $\beta = 0.5$, 5 different planet masses.	66
C.2	Clockwise, $\beta = 1$, 5 different planet masses.	67
C.3	Clockwise, $\beta = 2$, 5 different planet masses.	68
C.4	Clockwise, $\beta = 5$, 5 different planet masses.	69
C.5	Clockwise, $\beta = 10$, 5 different planet masses.	70
C.6	Clockwise, $\beta = 15$, 5 different planet masses.	71

Chapter 1

Introduction

1.1 Exoplanets

Philosophers have long pondered the existence of planets beyond the solar system, orbiting stars other than our own. Ever since the first discoveries of these ‘exoplanets’ were made (Wolszczan & Frail 1992; Wolszczan 1994; Mayor & Queloz 1995), hunting them has remained an exciting task for astronomers. This interest is partly due to the implications for extraterrestrial life, which provide a profound scientific motivation for finding exoplanets. Recently, the rate of exoplanet discovery has increased dramatically, due to advances in observational technology and in particular the success of space missions such as *Kepler* (Borucki et al. 2010). Figure 1.1 shows a plot of the semi-major axes and masses of the known exoplanets at the time of writing, colour-coded by their discovery technique.

Exoplanets can be discovered through a number of different methods.

- The *Radial Velocity (RV)* method involves looking for Doppler shifts in the stellar spectra due to the motion induced by a planetary companion. This is particularly effective for edge-on orbits as the magnitude of the frequency shift in the light from the star will be maximised.
- The *Astrometry* method looks directly for the subtle stellar motion due to a planetary companion, by studying the star’s position over time with high precision astrometric measurements.
- The *Transit* method uses the slight dimming in light of a star due to a planet transiting in front of it as evidence of a planetary companion. A number of projects, such as MEarth (Irwin et al. 2009) and *Kepler* look for planetary transits using long-term, high-cadence photometric observation of specific target stars.

- *Gravitational Microlensing* is the method utilised in this study, and involves observing the brightening of a background star due to the gravitational influence of foreground planetary systems. This method is detailed further in §1.2 and §2.
- Other methods, such as *Direct Imaging* and *Timing*, can also be used in specific cases. Direct imaging involves observing light from an exoplanet directly. This light can either be reflected starlight or thermal emission from a young, self-luminous planet. Direct imaging is most sensitive to massive planets on very wide orbits, as these are removed from the glare of their host stars. Timing can discover exoplanets through a range of techniques such as precise timing measurements of pulses from pulsars (Wolszczan & Frail 1992) and variations in eclipse or transit timings (Ballard et al. 2011).

Table 1.1 summarises these methods together with the number of planets they have discovered. The recent success of the *Kepler* mission has resulted in an abundance of exciting new transiting planet discoveries, with exotic circumbinary planets (Doyle et al. 2011) and potentially habitable ‘Super-Earths’ (Borucki et al. 2012; Anglada-Escudé et al. 2012) being among the more notable examples.

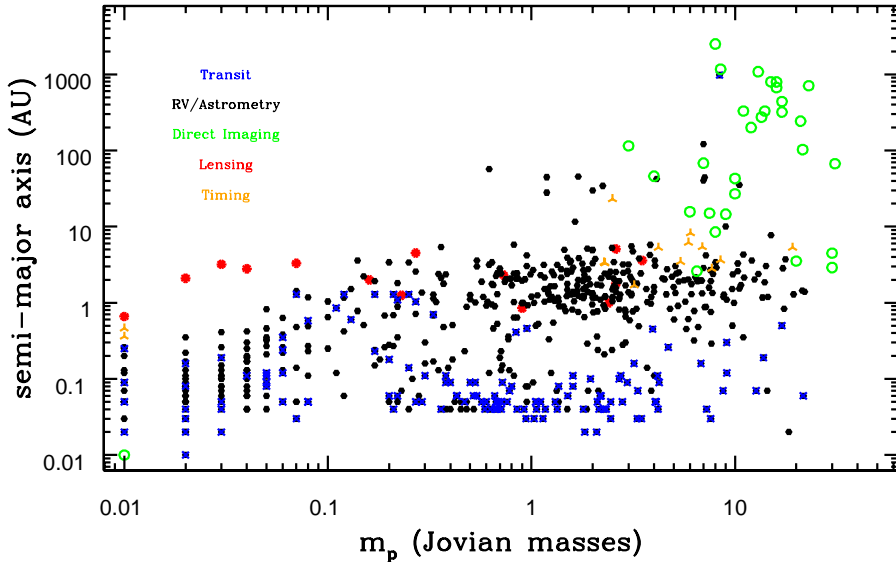


Figure 1.1: Known planetary orbits and the corresponding masses. Each point is colour coded according to its discovery technique. The lined appearance of the data at lower masses and separation is caused by the known precision of m_p and a for the specific planet. *Data courtesy of <http://exoplanet.eu>.*

Method	Number of Planets	Example
RVs / Astrometry	469	51 Peg b (Mayor & Queloz 1995)
Transits	230	GJ1214b (Charbonneau et al. 2009)
Microlensing	15	OGLE-06-109L b (Wang & Zhou 2011)
Direct Imaging	31	Fomalhaut B (Kalas et al. 2008)
Timing	16	PSR B1257+12a (Wolszczan & Frail 1992)

Table 1.1: A summary of the exoplanet detection techniques and total numbers of discoveries from each method at the time of writing. *Data courtesy of <http://exoplanet.eu>.*

1.2 Gravitational Lensing and Microlensing

As massive objects in the sky execute their complex celestial dance routines they will inevitably pass in front of background stars. Einstein’s theory of General Relativity (GR) (Einstein 1916) predicts that a massive body’s gravitational field will modify the geometry of spacetime, meaning that geodesics (lines along which the distance between two points is at a minimum) can be curved. Free particles (including photons) move along geodesics, so massive objects will cause light to ‘bend’ around them.

Originally, Einstein postulated that the magnitude of the deflection associated with the effect would be in accordance with Newtonian gravity’s effect (Einstein 1911), but later noticed that GR required a modification of this deflection to account for the general principle of equivalence (Einstein 1915). The deflection of light due to a gravitational field, gravitational lensing, was first confirmed experimentally by Dyson et al. (1920). They observed shifts in the positions of background stars during the 1919 solar eclipse, due to the effect of the Sun’s gravitational field on the path of light.

As a result of this deflection, lensing causes a magnification in the light from the source, analogous to the focusing of light rays through a traditional glass lens. A given source has a constant surface brightness, but lensing causes the object to take up a greater area on the sky. This results in a magnification in apparent brightness by a factor A . Gravitational microlensing is a subset of lensing where the astrometric shift in the position of the source is too small to be resolved, but the brightening effect of gravitational lensing can still be observed. It was first discussed by Einstein (1936). Despite Einstein’s fear that the effect would never be observed, as the observer would be ‘dazzled’ by the light from the lens star, microlensing observing teams now observe ~ 1500 events per year.

If a foreground mass passes in front of a background source it produces a magnification over time. To search for exoplanets, observing teams look for perturbations in this standard single lens light curve which may be caused by the lensing

effect of a binary system. At the time of writing, the Gravitational Microlensing technique has discovered 15 exoplanets. The current generation of lensing surveys, such as OGLE¹ and MOA² are used to flag events, and these are then followed up by teams such as the μ FUN³ and PLANET⁴ collaborations. Gravitational microlensing offers unique capabilities compared to other exoplanet detection methods. It can detect planets in all orbital orientations and is capable of finding planets orbiting dim stars. It is also possible to conduct exoplanet microlensing searches in tandem with other studies. Microlensing has typically been most sensitive to planets lying beyond the habitable zone (Sumi et al. 2010). However, recent work has shown that it can detect planets with a wide range of orbital separations (Di Stefano 2011; Di Stefano et al. 2012a; Di Stefano et al. 2012b).

1.3 Principal Objectives

The work presented here expands upon traditional lensing surveys in the following ways:

1. We consider lensing events that are predicted in advance.
2. We study the nearby stellar population to identify lensing candidates. We use an event produced by the low-mass star VB 10 as a case study.
3. We confirm that it is possible to detect planets in a range of orbital separations (see §2.3.1).
4. We assess the prospects for future events, using the *Kepler* field as an example.

One of the aims of this study is to suggest to the lensing and exoplanet communities that lensing is sensitive to a wider range of planetary orbits than considered before. At the commencement of this work, the prediction of the VB 10 lensing event by Lépine & Di Stefano (2012) had just been made. It is studied in depth in §3, and §4 contains a discussion on the prospects for predicting events in the *Kepler* field. The required theoretical background is discussed in §2.

¹<http://ogle.astrouw.edu.pl/>

²<http://www.phys.canterbury.ac.nz/moa/>

³<http://www.astronomy.ohio-state.edu/~microfun/>

⁴<http://planet.iap.fr/>

Chapter 2

Theoretical Background

2.1 Lensing Theory

To distinguish between the gravitational lensing signatures of systems with and without planets it is important to understand in depth the behaviour of both single and binary lenses. First we consider a single lens of mass M at a distance D_L and a source star S at a distance D_S . If we define $\theta = \theta_S + \theta_I$ from this arrangement (shown in figure 2.1), then

$$\theta D_S = \theta_S D_S + \theta_D (D_S - D_L) \quad (2.1)$$

where θ_D is the deflection angle, given by

$$\theta_D = \frac{4GM}{D_L c^2 \theta} \quad (\text{Mollerach \& Roulet 1978}) \quad (2.2)$$

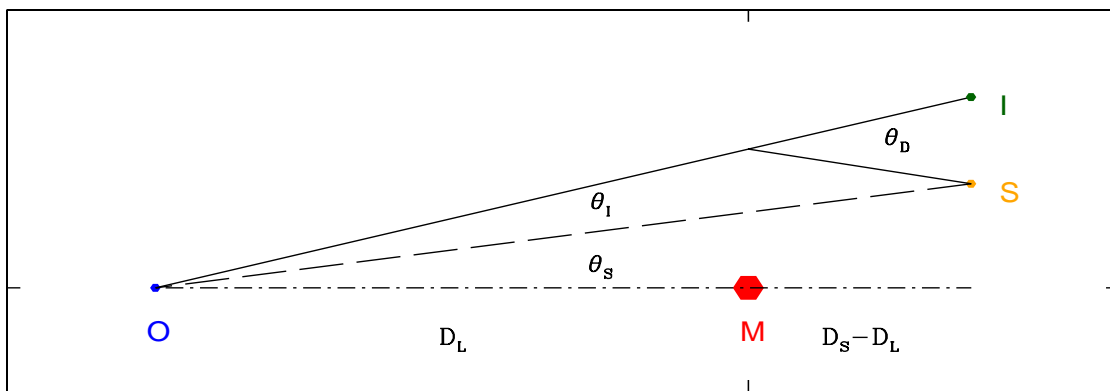


Figure 2.1: Geometry of a point-mass lens

If we substitute equations 2.1 and 2.2 into the lens equation, $\theta_S = \theta - \theta_D$, then we obtain

$$\theta^2 - \theta_s\theta - \theta_E^2 = 0; \quad (2.3)$$

$$\theta_E = \sqrt{\frac{4GM(1-x')}{D_L c^2}} \quad (2.4)$$

where $x' = D_L/D_S$. θ_E is the ‘Einstein angle’ of the lens, which is the value of θ when lens, source, and observer are aligned and corresponding angular size of the ‘Einstein ring’ image produced. Solving equation 2.3 for a given source position results in two solutions for θ , which are the positive and negative parity images at angular positions of θ^+ and θ^- :

$$\theta_{\pm} = \frac{\theta_S}{2} + \theta_E \sqrt{1 + \frac{\theta_S^2}{4\theta_E^2}} \quad (2.5)$$

Note that when we consider lensing by a stellar mass at a distance on the order of parsecs then the separation is of the order of milliarcseconds (mas). This means the images are too close to be resolved and are said to be in the regime of microlensing. The lensing process produces a deflection vector, $\vec{\theta}_D$ (the vectoral generalisation of θ_D), and similarly the positions of the actual source and images are given by $\vec{\theta}_S$ and $\vec{\theta}$, then the magnification factor A can be expressed as

$$A = \frac{d\Omega'}{d\Omega_0} = \frac{1}{\det J} = \frac{\partial \vec{\theta}_S}{\partial \vec{\theta}} \quad (2.6)$$

where $d\Omega'$ and $d\Omega_0$ are the observed solid angle and the solid angle without lensing. J is the Jacobian of the lens mapping and relates the two by $d\Omega' = (\det J)^{-1} d\Omega_0$. By summing over both images (equation 2.5) we have the equation for the magnification of a single lens:

$$A = \frac{u^2 + 2}{u\sqrt{u^2 + 4}} \quad (2.7)$$

where $u = \theta_s/\theta_E$. By inspection, we see that when the source lies at an angular distance equal to the characteristic scale of lensing events, θ_E , then $A = \sqrt{5}/3$. This is roughly equivalent to a 34% magnification.

For binary lenses, the treatment is somewhat more complicated. We start by expressing the positions of the source (ζ) and image (z) in complex coordinates (Witt 1990), and then can derive the lens equation

$$\zeta = z - \frac{\mu_a}{\bar{z} - \bar{z}_a} - \frac{\mu_b}{\bar{z} - \bar{z}_b} \quad (2.8)$$

where $\mu_i = m_i/m_{tot}$ and z_i is the position of lens i . This equation can be recast as a 5th order polynomial, whose solutions are the positions of the images (see Mollerach & Roulet (1978) for the formalism). These solutions are obtained using numerical methods, and then the magnification can be calculated with equation 2.6. The computational routine for doing this is described in §3. Usually, two of the solutions to the polynomial are spurious and only three images are produced. However, if $\det J = 0$ then the magnification diverges and the source is said to lie inside a ‘caustic curve’. In the case of a true point source this would result in a non-physical, infinite magnification, but with a source with a physical, finite size this results in a finite magnification (Penny et al. 2011b). In this case five, rather than three images are produced and there is a dramatic increase in magnification. High magnification events where the caustic curves pass over the source on the sky are known as ‘caustic crossings’. These are the types of event that have generally been looked for with microlensing surveys so far, as they are the easiest signatures of binary lenses to detect.

To pass close to one another, the lens and source have a relative proper motion. This will affect the timescale of an event. If μ is the proper motion of the lens relative to the source in angular units, we can define τ_E , the time it takes for the lens to travel $2\theta_E$ (the Einstein diameter crossing time) as

$$\tau_E = \frac{2\theta_E}{\mu} = \frac{4}{\mu} \sqrt{\frac{GM(1-x')}{D_L c^2}} \quad (2.9)$$

Finally, let b , the angular distance of closest approach help us define

$$\beta = \frac{b}{\theta_E} \quad (2.10)$$

We can now start to consider some characteristics that differentiate this program from traditional lensing surveys.

2.2 Mesolensing

Mesolensing is defined as high-probability microlensing (Di Stefano 2008a). Mesolensing by nearby stars offers a number of advantages over traditional microlensing studies (Di Stefano 2008b). First, the nearby stellar population ($d \lesssim 500$ pc) is well studied and catalogued, meaning that the proper motion may be known and mass and distance estimates may be available. Second, being nearby means that their Einstein angles and proper motions are large, so they will cause more lensing

events per unit time than stars further away. Catalogues such as LSPM-north (Lépine & Shara 2005a) have identified numerous high proper motion stars, and provide a perfect resource for identifying candidate mesolenses.

Mesolensing studies also offer one crucial advantage regarding follow-up observations. Typically, planets discovered by lensing have degeneracies associated with them. This is because it is not always possible to independently determine mass ratios and orbital characteristics due to the nature of studying lensing light curves. Being nearby means that RV, direct imaging and astrometry follow-up may be possible and we may be able to break these degeneracies.

2.3 Detecting Planets

When exoplanet microlensing was first discussed (Mao & Paczynski 1991; Gould & Loeb 1992), attention focused on the *Resonant* regime. This is the regime of approaches when the orbital separation is comparable to θ_E and caustic crossings can occur. In this regime it is possible to observe high magnification events ($A > 3$), with sharply increasing, wall-like caustic structures in the light curve (Griest & Safizadeh 1998).

Figure 2.2 shows the light curve which led to the discovery of two planets: OGLE-2006-BLG-109Lb and OGLE-2006-BLG-109Lc (Gaudi et al. 2008). The sharp, high-magnification caustic features can be seen in separate, distinct locations on the light curve, and are associated with the caustic structures in the numbered regions. The inset plot shows the path of the source relative to the lens caustic curves in the model fitted to the data, with the numbers corresponding to points on the light curve. This plot gives a good indication of the general procedure for discovering planets so far with microlensing. High magnification events are flagged by the monitoring team (in this case, OGLE), with high cadence, near-continuous follow-up carried out by a network of other teams (marked in different colours on the figure).

2.3.1 Other Types of Planet-Lens Signatures

In addition to the high magnification caustic crossing events associated with the 15 exoplanets discovered with microlensing, it is also possible to discover planets in a range of orbital separations. We can define α , the orbital separation of a planet in units of the host star's Einstein radius.

$$\alpha = \frac{a}{R_E} \tag{2.11}$$

where a is the orbital separation and R_E is the Einstein radius (the physical size of the Einstein angle) given by

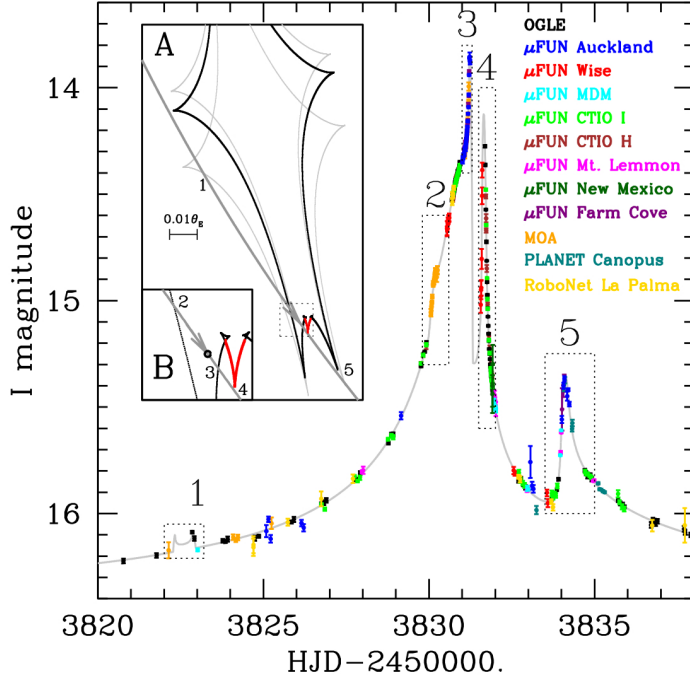


Figure 2.2: The light curve for microlensing event OGLE-2006-BLG-109L. Image credit: Udalski et al. 2005- <http://www.astronomy.ohio-state.edu/~microfun/ob05071/>

$$\frac{R_E}{1\text{AU}} = \theta_E \frac{D_L}{1\text{pc}} \quad (2.12)$$

Di Stefano (2011) showed that close-orbit planets with masses as low as the Earth's can produce noticeable quasiperiodic deviations, which are maximised when the source lies at an angular distance

$$\theta_\alpha = \left(\frac{1}{\alpha} - \alpha \right) \theta_E \quad (2.13)$$

from the centre of mass of the binary system. In addition, Di Stefano & Scalzo (1999a; 1999b) examined the potential for detection of wide-orbit planets by microlensing, where the planet produces a lensing effect independently of the host star due to its own individual Einstein angle passing close to the source star. It is also possible to detect short-duration events caused by objects such as ‘free-floating’ planets (Di Stefano 2009a; Di Stefano 2009b). Both wide and close orbit planet effects are discussed further in §3 in application to the predicted VB 10 event.

2.3.2 Inclination and Eccentricity: Orbital Elements and Their Effect on Lensing

An orbit is described by its orbital elements (Cassen 2006):

- eccentricity (e)
- semi-major axis (a)
- orbital period (P)
- inclination (i)
- longitude of ascending node (Ω)
- argument of periapsis (ω)
- planet mass (m_p).

It is pertinent here to also define the mass ratio $q = m_p/m_{tot}$, where m_{tot} is the total mass of the system. Figure 2.3 illustrates the geometry of an inclined orbit, where the plane of reference would be face-on to the observer. The effects of orbital orientation are explored further in §3.5.2. Eccentricity has more subtle effects, that are not explored in the simulations here. We are interested in studying the signatures of planets, and exploring the possibility of prediction. Elliptical orbits behave differently to circular ones during lensing events, but being as the planet will still spend most of its time close to aphelion, the effect of eccentricity on the types of lensing signatures we consider here is minimal. We have thus chosen to use circular orbits as an approximation throughout. It should be noted that, should a planet be discovered through any of the predictions made here, eccentricity would, of course, have to be taken into account. The fitting of eccentric orbits to lensing events is well understood (see, e.g., Wang & Zhou 2011), and has been undertaken for planets discovered with microlensing.

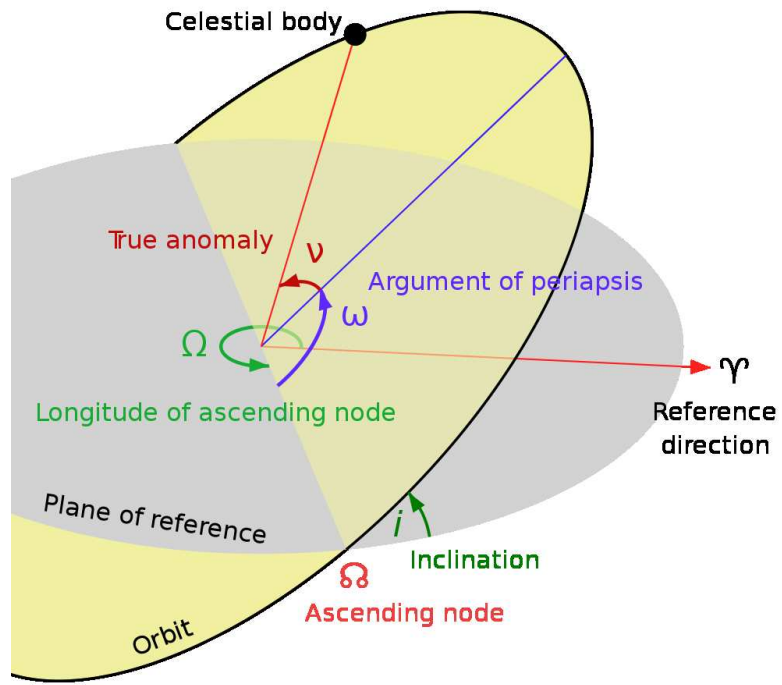


Figure 2.3: The geometrical quantities defining an orbit outlined, with some of the orbital elements marked. The reference plane is taken to be a face-on orbit (i.e. the observer is looking from below). *Image credit:* <http://lasunnty.110mb.com/>

Chapter 3

The VB 10 Predicted Mesolensing Event

VB 10 is a high proper motion (HPM) dwarf star, discovered by Van Biesbroeck (1944). VB 10 is an intriguing star for a number of reasons. With an estimated mass of $0.07 - 0.08 M_{\odot}$ (Pravdo & Shaklan 2009), it lies close to the mass boundary between brown dwarfs and nuclear-burning stars (Chabrier et al. 2000; Richer et al. 2006). VB 10, category M8V, is also extremely red, with apparent magnitudes in K and B band of $m_K = 8.76$ and $m_B = 19.2$ respectively (Cutri et al. 2003a; Lépine & Di Stefano 2012).

In a lensing context, VB 10 is an interesting candidate due to its proximity. It is located at a distance of 5.82 pc, which leads to a large Einstein angle (see equation 2.4) of $\theta_E = 10$ mas. Coupled with its proper motion of $1.5''\text{yr}^{-1}$, this means that VB 10's Einstein angle sweeps out a relatively large area on the sky in a given time (Lépine & Di Stefano 2012). This makes it an ideal target for mesolensing studies, as the probability of lensing events will be higher compared to stars with smaller Einstein angles.

3.1 A Prediction, its Implications, and Challenges

It was noticed that VB 10 was due to pass in front of a background star, dubbed [VB 10]-PMLS-1 (the VB 10 *Predicted MesoLens Source*). This prediction is discussed in Lépine & Di Stefano (2012). By studying two *Hubble Space Telescope* (*HST*) epochs of the field around VB 10 (see figure 3.1), they were able to make an initial prediction of December 7th 2011 as the day of closest approach, with a distance of closest approach of $b \approx 50$ mas ($\beta \approx 5$).

This initial prediction was refined once it became apparent that uncertainties in the proper motion of the background star would mean that the time and distance of

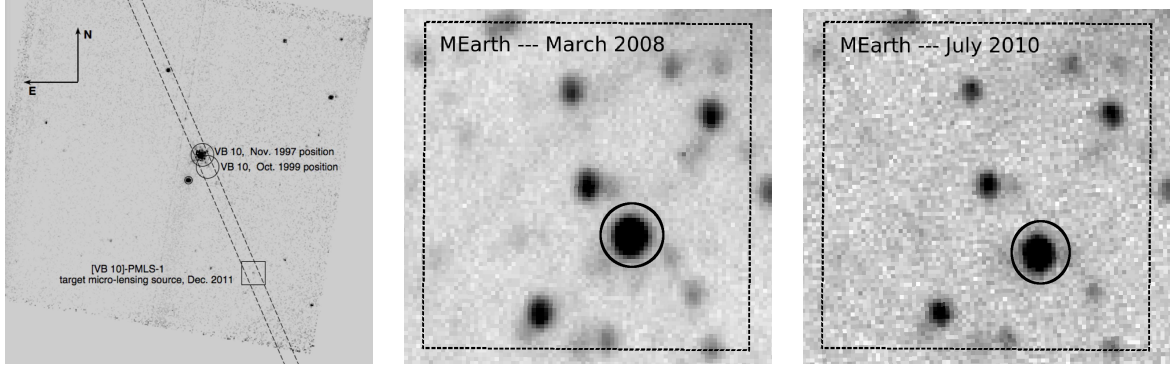


Figure 3.1: *Hubble Space Telescope* NICMOS (left) and MEarth (centre and right) images of the field around the nearby low-mass star VB 10. The position of VB 10 at two separate epochs is identified with an open circle in both cases. The proper motion of VB 10 is apparent and the source star, [VB 10]-PMLS-1, is labeled with an open box in the *HST* image.

closest approach were not known precisely. To determine the likelihood of different relative paths, a Monte Carlo simulation of 10^4 paths was carried out. This took the uncertainties into account using limits obtained from the two *HST* epochs to constrain the proper motion of [VB 10]-PMLS-1 and produce possible relative paths between the lens and source. Figure 3.2 shows the distribution of possible times of closest approach, and table 3.1 summarises the relative probabilities of the approach being closer than the closest approach of six example simulated paths. These paths are also illustrated in figure 3.3.

$\phi(\text{mas})$	$P(b \leq \phi)(\%)$	date of closest approach for that path
5	2.5	15 Jan 2012
10	4.9	5 Feb 2012
20	9.4	14 Jan 2012
50	22.6	20 Jan 2012
100	43.7	17 Jan 2012
150	62.7	1 Feb 2012

Table 3.1: Column 1: angular separation, ϕ , measured in mas. Column 2: probability that the angle of closest approach, b , between VB 10 and [VB 10]-PMLS-1 will be smaller than ϕ . Column 3: the date of closest approach for the specific path shown in Figure 4.3, with angle of closest approach approximately equal to ϕ .

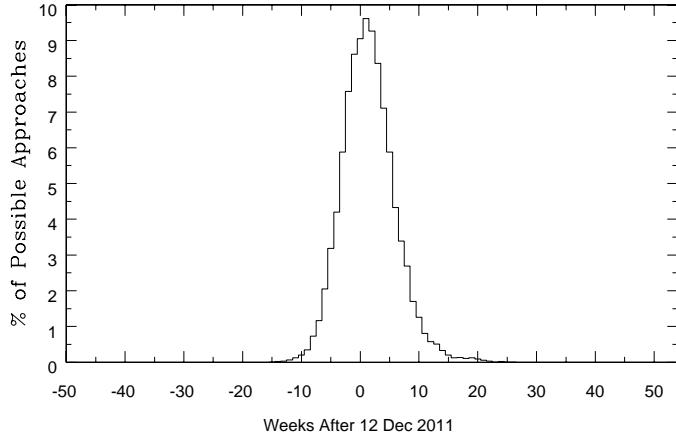


Figure 3.2: Probability distribution for the time of closest approach, derived from Monte Carlo simulations accounting for uncertainties in the astrometric motion of VB 10 relative to the background star. The data are binned according to week.

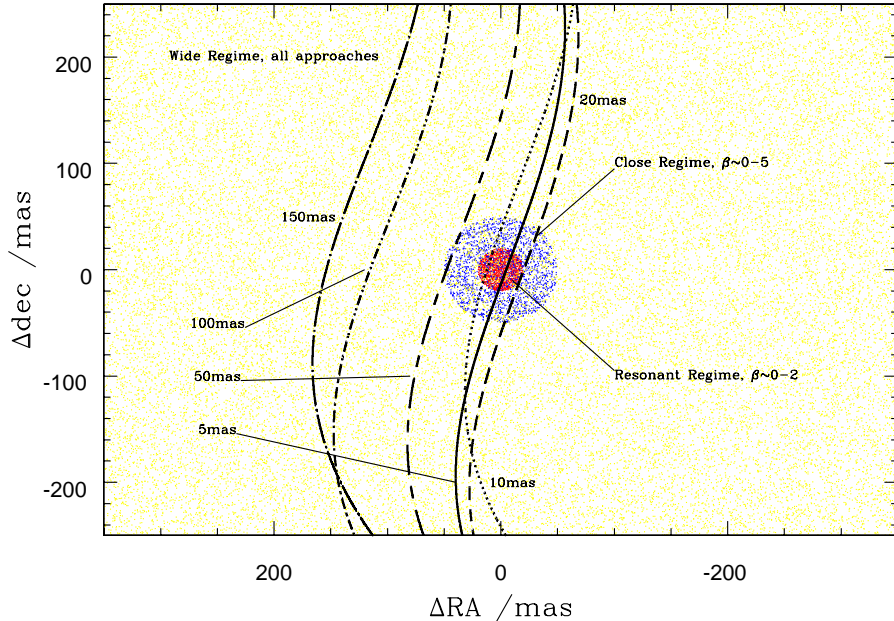


Figure 3.3: Six possible paths of VB 10 where $(\Delta\text{RA}, \Delta\text{dec})$ is the position in mas relative to [VB 10]-PMLS-1. The approximate angular distance of closest approach for each path is labeled, and the sinusoidal shape of the paths is due to parallax. Each of the three background colours corresponds to a β parameter space defining the type of planets that can be detected. Yellow, blue and red correspond to the wide, close and resonant regimes respectively (see §3.4).

3.1.1 Observational Difficulties

It is important to note that there are a number of factors that make the VB 10 event difficult to observe. The most fundamental difficulty lies in the relative magnitudes. The background star is very dim compared to VB 10, meaning that the blending of light will make lensing more difficult to detect. The B,I and H band magnitudes of [VB 10]-PMLS-1 are estimated to be $m_B \simeq 21.0$, $m_I \simeq 18.2$ and $m_H \approx 16$ (Lépine & DiStefano 2012). We can thus estimate the blended magnitude

$$m_{blend} = -\log_{2.512}(2.512^{-m_l} + 2.512^{-m_s}) \quad (3.1)$$

where m_l and m_s are the apparent magnitudes of the lens and source respectively. The blended apparent magnitude in B band is $m_{blend,B} \simeq 19.25$. When a source is magnified by a ‘true magnification’ of $A(u)$, only a fraction, f , of its luminosity in a given band is actually magnified (Di Stefano & Esin 1995). This fraction is wavelength dependent. Taking this into account, the change in magnitude of the background star due to a lensing magnification is

$$\Delta m = -\log_{2.512}(fA(u)) \quad (3.2)$$

This leads to a blended magnitude of $m_{blend,B} \simeq 19.23$ when $fA(u) = 1.01$ (an observed 10% magnification), highlighting some of the difficulties involved in this particular event. Nevertheless, with the right photometry it may still be possible to detect planets, and even if no planets are detected we can learn something from the event if the approach is close enough.

VB 10’s variability (Cutri et al. 2003a; West et al. 2008; Hilton et al. 2010) also poses challenges. VB 10 is an active M dwarf and is known to exhibit flares. It is important to be able to distinguish lensing signatures from possible flare activity. For this we must rely on multi-waveband observations (see §3.6) and the fact that flares have a characteristic fast rise and exponential decay. Although rotation effects can affect flare signatures (Berger et al. 2008), we expect to be able to distinguish lensing from flare activity by considering the shape and timescale of the events.

One additional challenge associated with observing VB 10 is its rather difficult position on the sky around closest approach, which made it impossible to observe for December 2011 and January 2012. This accounts for a gap in the data collected during the event (see §3.6). Figure 3.4 shows the angle between the sun and VB 10 on the sky (the solar angle) as a function of time, with the closest angle that *HST* can observe marked with a line.

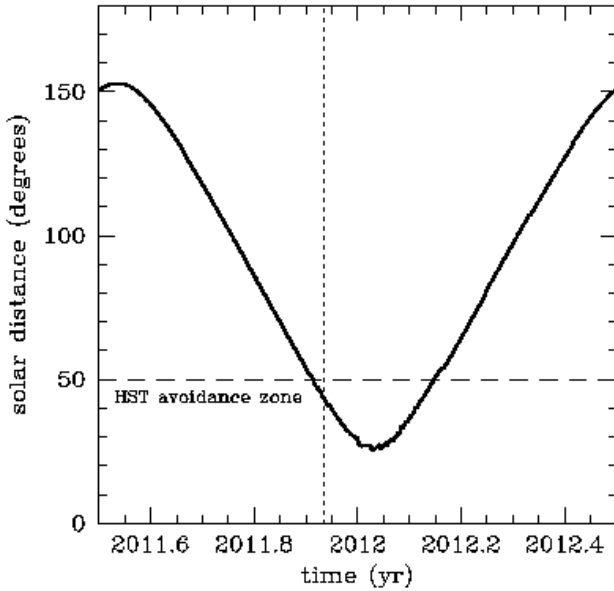


Figure 3.4: The angle between the sun and VB 10 on the sky (the solar distance) as a function of time, with the smallest angle that *HST* can observe at marked with a horizontal dashed line. Observing conditions are at their worst around January 2012- unfortunately close to the most likely time of closest approach which is marked with a vertical dotted line. *Figure credit: Lépine & Di Stefano (2012).*

3.2 Does VB 10 Have Planets?

Several searches for planets around VB 10 have been conducted. A planet of $6.4(+2.6, -3.1)$ Jupiter-masses (M_J) and a period of $0.744(+0.013, -0.008)$ yr (about 271 days) was proposed to have been the first around any star to be discovered by astrometry (Pravdo & Shaklan 2009). Pravdo and Shaklan fitted the observed data with a parallax and proper motion (PPM) model, and found that the probability of this describing the motion with no additional perturbations was very low. A PPM model combined with a Keplerian two-body model with the parameters above fitted the observed data well and thus the planet discovery was announced. Subsequent papers have ruled out the $6.4M_J$, 271-day planet, with various limits being placed on the possible parameters of any planets that may orbit VB 10 (Anglada-Escudé et al. 2010; Bean et al. 2010; Lazorenko et al. 2011). Lazorenko et al. rule out the existence of $6.4M_J$ and $3.2M_J$ planets on the 271-day orbit with low false alarm probabilities using astrometry, and Anglada-Escudé et al. place an upper limit of $m \sin i \sim 2.5M_J$ using RV measurements. Using high precision RVs, Bean et al. rule out masses greater than $3M_J$, and note that planets

down to one Jupiter mass would have to have unusually large eccentricities (> 0.7) to elude detection.

These limits do not rule out the possibility that VB 10 has planets, and there is evidence that low-mass stars are good candidates as planet hosts. The low-mass M dwarf GJ 581 is the star with the largest number of confirmed planetary companions (Mayor et al. 2009) and a massive planet orbiting an M dwarf was recently discovered with microlensing (Batista et al. 2011).

3.3 Method: Computer Simulations

To simulate a lensing event it is required to compute the magnification of a binary lens. A well-tested FORTRAN code developed by Shude Mao was used for this purpose. This code has been used in a number of publications (see, e.g., Mao & Paczynski 1991), but the code itself is not public. The function $mag(x, y, x_1, y_1, x_2, y_2, m_1, m_2, n_r)$ carries out the following steps in order to model binary lens effects:

1. We specify the source position (x, y) , positions of both lenses (x_1, y_1) and (x_2, y_2) and lens masses m_1 and m_2 . Masses should be in terms of fraction of total mass, and positions in units of θ_E . The variable n_r is returned by the code and corresponds to the number of images, or real solutions to the fifth order polynomial.
2. These positions are expressed in complex coordinates as in equation 2.8, with the positions translated such that the first lens is at the origin.
3. The lens equation is recast as a fifth order polynomial, and solved using *Mathematica* coefficients and the numerical recipes subroutine *zroots*.
4. If the solution is real and thus corresponds to an image, the magnification is computed and summed over all real images.

This function can then be used to study the lensing signatures of any moving system in which a binary lens passes in front of a background star. The general procedure to derive light curves is to set the centre of mass along a given path, and by specifying the mass ratio q , α , phase and the orbital elements we can investigate the possible lensing signatures for any binary lens event by modeling motions on the sky. Appendix A contains a printout of a code written during this project to carry out this procedure, as well as identifying peaks in the deviation from single lens behaviour that might be indicators of planets. Further details on the procedures for calculating the magnification of binary lenses can be found in Schneider & Weiss (1986) and Witt (1990).

Specifically concerning the VB 10 event, we have computed 50,000 light curves for circular, face-on orbits (clockwise and counterclockwise) in which initial phase and α were sampled randomly. This was done each time for five different planet masses (3 Jupiter, Jupiter, Saturn, Neptune and Super-Earth) and six sample paths (see §3.1), leading to 30 completed simulations. A Super-Earth is taken to be a planet of 5 Earth-masses. More detail on these simulations and their results is presented in §3.5 and two papers (Di Stefano et al. 2012a; Di Stefano et al. 2012b). The effects of orientation and inclination on the simulation results have been considered (see §3.5.2).

3.4 Three Orbital Regimes

To examine the photometric signatures of planets we have simulated lensing light curves produced by planetary systems, using the well-tested code described in §3.3. So as to carry out the analysis in time for it to be useful to potential observers, we considered only circular face-on orbits, which allowed us to study the key effects. In §3.5.2 the possible effects of the orbital orientation have been considered, as well as in the treatment of wide orbit planet probabilities (§3.4.1). The type of lensing signature produced depends on the lensing “regime” associated with each event. The lensing regime is defined by two parameters; α and β , as introduced in §2. The type of lensing and probability of detection in each regime varies significantly with these parameters, and the approximate boundaries of the three regimes are defined in table 3.2. Figure 3.5 shows typical lensing signatures produced by planets that are detectable in each lensing regime.

Regime	β	α	Panel in figure 3.5
Wide	<i>all</i>	~ 2.0	Top
Close	~ 5.0	~ 0.5	Middle
Resonant	~ 2.0	$0.5 - 2.0$	Bottom

Table 3.2: A summary of the properties of the three different regimes outlined in §3.2. α is the orbital separation in units of θ_E and β is the distance of closest approach in units of θ_E .

3.4.1 The Wide Orbit Regime

Wide orbit planets can be detected in the wide orbit regime, which covers all distances of closest approach less than the maximum orbital separation. This can be expressed by considering the effect of a hypothetical planet on the well-studied astrometry of VB 10. If VB 10 has a planet of mass m_p , with a maximum

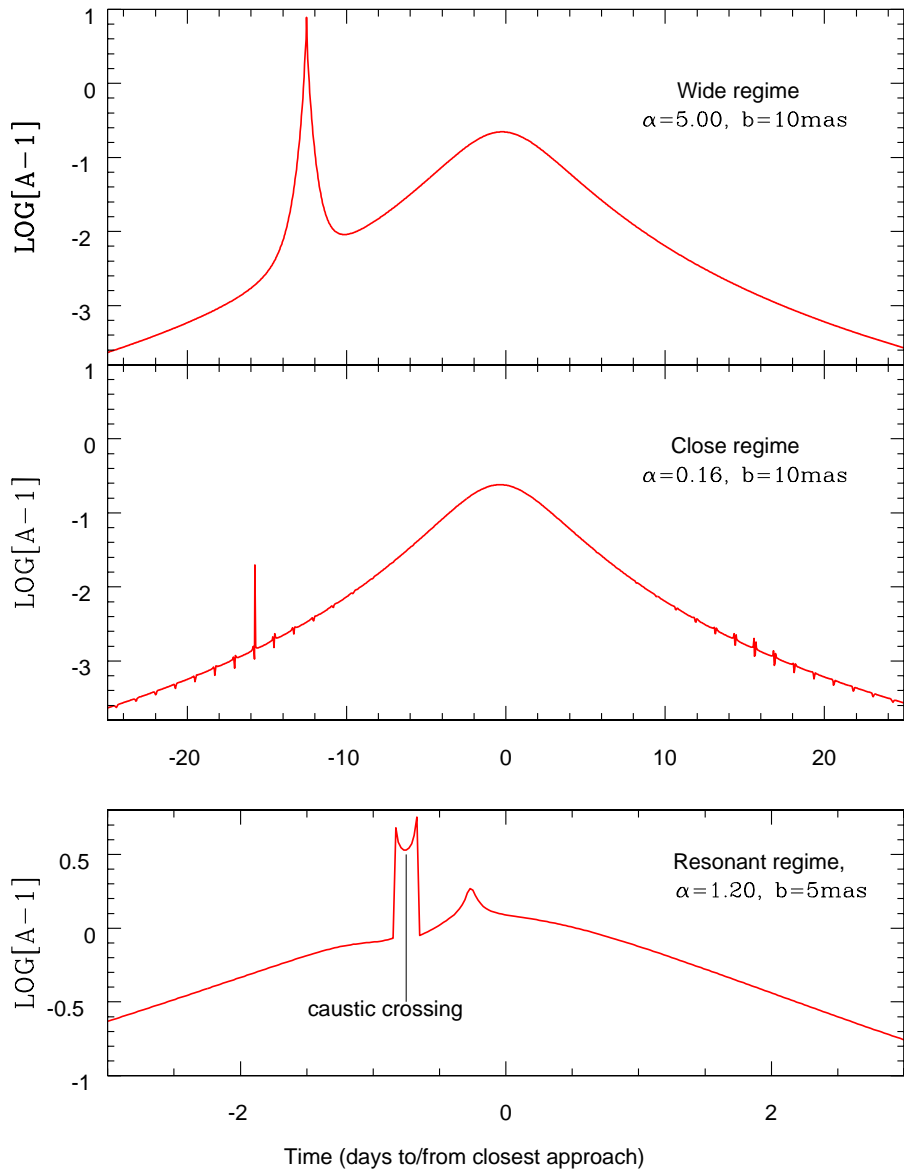


Figure 3.5: Light Curves showing the types of effects produced by planetary systems in wide orbits (top), close orbits (middle) and orbits in the zone for resonant lensing (bottom). Whilst each type of orbit produces very different effects, it is possible to detect planets in a range of different orbits with the correct cadence and photometry. The wall-like magnification features associated with a caustic crossing can be seen clearly in the bottom panel.

separation from the centre of mass of a_{max} , then VB 10 has a maximum separation a_* from the centre of mass of $a_* = a m_p/M_*$. There are, however, limits on the value of a_* which can be derived from the astrometric limits of Lazorenko et al. (2011). Specifically, if a planet of $6 M_J$ in a 271 day orbit is ruled out, then the maximum separation between VB 10 and the centre of mass is $\delta_* \sim 5 mas$. Taking this as a guideline, the maximum orbital separation of the planet can be expressed as follows.

$$a_{max} \sim 2.18 AU \frac{\delta_*}{5 mas} \left(\frac{M_*}{0.075 M_\odot} \right) \left(\frac{0.001 M_\odot}{m_p} \right) \quad (3.3)$$

At the distance to VB 10, this corresponds to a maximum angular separation between a Jupiter-mass planet and VB 10 of about $0.38'' = 38\theta_E(\beta = 38)$.

In the wide regime, the regions of deviation in magnification around the planet are substantially separated from that of the host star (see the plot of isomagnification contours in figure 3.6). The isomagnification contours move across the sky in motion around the centre of mass, meaning that the region of deviation can pass in front of the source star on the sky. Wide orbit planets can therefore produce events independently of the stellar event, which will be seen as peaks in the light curve at a given time before or after the main event, as the planet passes close to the background star on the sky (see §3.8). We can assess the probability of this happening for a hypothetical planet with geometrical arguments.

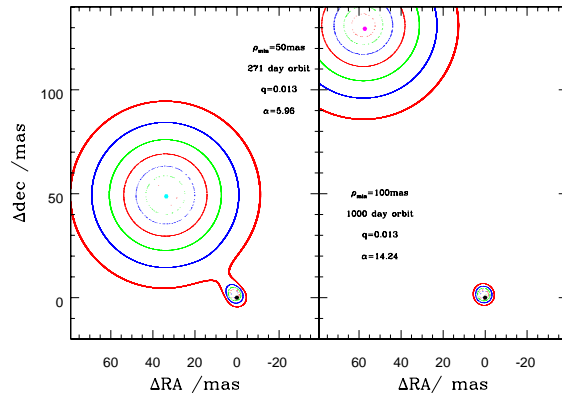


Figure 3.6: Isomagnification contours for two different wide orbits. The position on the sky of both the planet and the source star is $(0, 0)$. The outer blue contour corresponds to a magnification $(A - 1) = 0.01$, and the magnification associated with each contour increases by a magnitude increment (a factor of ~ 2.5) as they get closer to the lens. Note that the isomagnification contours associated with the planet are significantly influenced by VB 10 for $\alpha = 5.96$; for the wider orbit the effect of VB10 on the region around the planet is smaller.

Wide-orbit Planet Probabilities

Consider a lens star, mass M_* , with a hypothetical wide-orbit planet, separation a , mass m_p approaching a background star, with an angular distance of closest approach, b . If the orbit is circular and face-on then the probability, P , of detecting an independent wide orbit planet during a stellar lens event (as derived in appendix B) is given by:

$$P(\alpha, \beta, \omega_f, \mu) = \frac{1}{\pi} \arccos \left(\frac{2\alpha^2 + 2\rho_{mag}^2 - x^2}{2\alpha^2 - 2\rho_{mag}^2} \right) + \frac{\omega_f x}{2\pi\mu} \quad (3.4)$$

where $x = \sqrt{(\alpha + \rho_{mag})^2 - \beta^2} - \sqrt{(\alpha - \rho_{mag})^2 - \beta^2}$, μ is the proper motion of the lens system and ω_f is the angular frequency associated with the planet's orbit, which can be positive or negative. ρ_{mag} is defined as the radial angular size of the region of a given perturbation, δ , around the planet, in units of the star's Einstein angle.

Whilst a generalised derivation of probability for all inclinations is difficult, this can be obtained more easily from simulations (as is done in §4). We can consider certain cases, such as edge on orbits, as a way to properly understand the geometry behind the simulation results. For example, if $i = \pi/2$ and Ω is varied, we have an expression for P which is valid when the condition $\alpha \geq \beta \cos \Omega - \rho_{mag}/2$ is satisfied:

$$P(\alpha, \beta, \omega_f, \mu) \approx \frac{1}{\pi} \arccos \left(\frac{\alpha + \rho_{mag}}{\alpha - \rho_{mag}} \right) + \frac{\omega_f x}{2\pi\mu} \quad (3.5)$$

The derivation for this expression is also given in appendix B.

The Size of the Region of Deviation

In the derivation above we defined ρ_{mag} to be the radial size of the region of a given perturbation, δ . An expression for ρ_{mag} as a function of δ , q and α has not been derived analytically. However, we can obtain approximate relationships based on simulation work. The amount of distortion in the region around the planet clearly varies significantly with α , and in some regimes the region is enclosed within the same corresponding contour around the star itself.

Figure 3.7 shows the variation in radial size of the region of a given perturbation, δ , as a function of α , for three values of q . Using these relationships we can estimate the functional form of ρ_{mag}

$$\rho_{mag}(q, \alpha, \delta) \sim F(\alpha, \delta) \rho_{pl,0}(q, \delta) \sim \left(\frac{1}{\alpha - \alpha_{crit}} + 1 \right) \rho_{pl,0}(q, \delta) \quad (3.6)$$

where α_{crit} is the value of alpha for which the planetary contours are no longer separated from the stellar contours. This is a function of both q and δ . $\rho_{pl}(\delta)$ is the size of the region enclosed by the corresponding isomagnification contour for an isolated single planet lens, and can be obtained numerically from equation 2.7 by considering the planet as a single lens. The above equation will only hold in the regime where the isomagnification contour considered is separated from the corresponding stellar contour, when $\alpha > \alpha_{crit}$. For specific predictions it is beneficial to run simulations to determine ρ_{mag} in each case, but this formula provides a good guide and helps us understand the dependence of probability on orbital parameters.

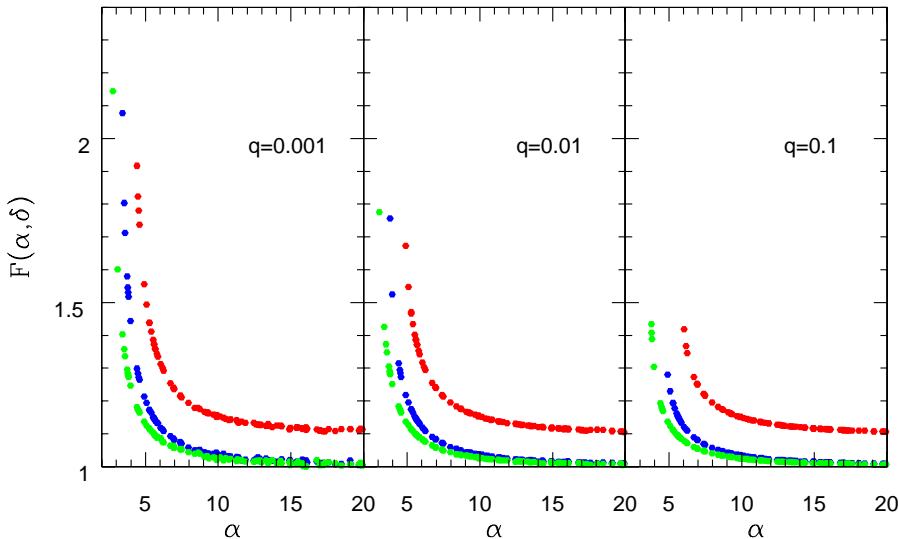


Figure 3.7: The value of $F(\alpha, \delta)$ as a function of α , where the red, blue and green curves correspond to $\delta = 0.1, 0.25, 0.625$ respectively. The factor F governs the size of a region of deviation in units of the planet's Einstein radius. The rough form of these relationships is described by equation 3.6.

Wide-orbit planets around VB 10

It follows from the arguments above that there is a specific value of α associated with a given time of event. Although parallax plays a part in the lensing signatures associated with the VB 10 event, we can derive a relationship between the event time and the orbital parameters by considering a straight line approach between lens and source. Let t_0 be the time of closest passage between VB 10 and the background star. If the time is expressed in days, and the proper motion μ is express in units of θ_E/day , then

$$\left| t - t_0 \right| = 2.5 \text{ days} \left(\frac{0.4 \theta_E \text{ day}^{-1}}{\mu} \right) \left(\alpha^2 - \beta^2 \right)^{\frac{1}{2}} \quad (3.7)$$

This relationship is plotted in figure 3.8 together with results from simulations, showing that there is a good agreement between the two. Equation 3.7 can be used to identify the type of planetary orbit that might be possible to observe on a given day. The timescale of the event can be estimated, and an observation can be tailored to suit by considering the photometry and cadence required. This ‘day-by-day guide’ can also be produced for the close orbit regime.

3.4.2 The Close Orbit Regime

If VB 10 happens to have planets with orbits smaller than the Einstein radius, the lensing signatures can also be significantly perturbed. This is because there is a small region within which the isomagnification contours are distorted from the circular form they would have had in the absence of the planet. Di Stefano (2011) contains further details. θ_α (see §2.3.1) can be as large as several times θ_E for $\alpha \ll 1$. In the absence of orbital motion, there would be only a small probability that the distorted region would pass in front of the source. However, for small values of α the orbital period is short, so there can be a good chance that the distorted region will rotate in front of the source star, possibly even more than once. For example, a face-on circular orbit with $\alpha = 0.2$ would correspond to an orbital period around VB 10 of roughly 1.7 days.

Just as there is a largest orbital separation for a wide-orbit planet, there is a smallest orbital separation for a close-orbit planet. To avoid catastrophic tidal disruption a planet must satisfy the condition $r_h \gtrsim 2r_p$, where r_h is the Hill radius given by $r_h \approx a(\frac{m_p}{3M_*})^{1/3}$ (Hamilton & Burns 1992). Thus the minimum orbital separation of a planet around VB 10 is roughly given by

$$a_{min} \sim 0.3R_\odot \frac{r_p}{r_J} \left(\frac{M_*}{0.075M_\odot} \right)^{1/3} \left(\frac{0.001M_\odot}{m_p} \right)^{1/3} \quad (3.8)$$

This minimum orbital separation will give us the maximum distance of close approach, β_{max} , in the close regime by the equation $\beta_{max} = (\frac{1}{\alpha_{min}} - \alpha_{min})$, where $\alpha_{min} = a_{min}/R_E$. This corresponds to $\alpha_{min} \sim 0.03$ for the VB 10 case, but being as our simulations show that events would only be detectable down to $\alpha \sim 0.2$ (see figure 3.8) we set $\beta_{max} \approx 5$.

The behaviour described by equation 2.13 means that close-orbit planets can produce deviations before and after the time of closest approach. The time at which the deviations start is the time at which the region at R_α passes in front

of the source star. If t_{max} is the time in days at which deviations are maximised, then we have the analogue to equation 3.7 for close-orbit planets:

$$\left| t_{max} - t_0 \right| \sim 2.5 \left(\frac{0.4 \theta_E \text{day}^{-1}}{\mu} \right) \left(\left(\frac{1}{\alpha} - \alpha \right)^2 - \beta^2 \right)^{\frac{1}{2}} \quad (3.9)$$

In this case, the smaller the value of α , the longer the difference in time between the stellar-lens event and the planet-lens event, meaning that once again the time at which an event might be observed can be used to estimate the orbital separation and required photometry.

3.4.3 The Resonant Regime

Traditionally, lensing planet searches (such as those detailed in §2.3) have focused in the regime where caustic crossings occur. Caustic crossing produce high magnification events and are easier to detect. The bottom panel of figure 3.5 shows example light curves for the resonant regime- notable features are the sharp, wall-like increases in magnification, and the structure in each peak from the caustic structures associated with each lens.

3.5 Results from Simulations

The simulations carried out produced the results of Di Stefano et al. (2012a). Figure 3.8 shows the results of the simulations for a Jupiter-mass planet with $\beta = 5$. We see events in the three regimes described, as well as a high number of events due to the reflex-motion of the star described previously. The smooth, coloured curves show the predictions from equation 3.7 (magenta) and equation 3.9 (cyan), and confirm that the straight line approximation used gives a reasonable estimate of the times at which a given planetary separation can be observed. Orange points also show the orbital separations and times at which caustic crossings occur, producing five images and a dramatic increase in magnification. These types of events would be the easiest to detect, but in this case are unfortunately the least likely to occur. Figure 3.9 shows the fraction of events involving caustic crossings for $\beta = 0.5, 1$, and the distribution of timescales in these events. There is a dramatic increase in the number of caustic crossing events for lower β , as we would expect.

Appendix C contains the full catalogue of simulation results for clockwise orbits. They indicate the behaviour we would expect- as β increases we pass out of the resonant regime, and are also no longer able to detect the effects of reflex motion. Two wing shapes are all we see, which are events cause by independent planet effects and the close-orbit planet effects described by equation 3.9. For the largest

values of β it is only possible to detect planets in the wide regime, as we would expect.

Figure 3.10 summarises all these results for the wide and resonant regimes for the full range of planet masses and approaches. The data are binned by orbital separation and shows the probability of detecting a hypothetical planet in the given orbital separation bin during the VB 10 effect. It shows once again that the probability of detecting planets is highly dependent on α , β and q .

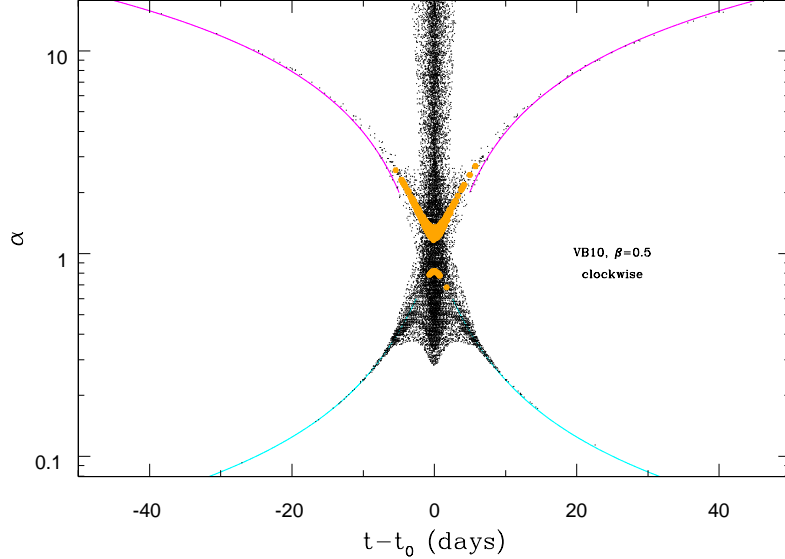


Figure 3.8: The logarithm of α , the orbital separation in units of R_E , versus $(t-t_0)$, where t_0 is the time of closest approach. For each point shown, t is the time of a peak in the photometric deviation $|A_{pl} - A_{pt}|$ from the single lens; we consider only those peaks with $|A_{pl} - A_{pt}| > 0.01$. The lens is VB 10 orbited by a hypothetical Jupiter-mass planet in a clockwise, circular face-on orbit. The distance of closest approach is $\beta = 0.5$. The smooth magenta curves that start in the upper corners of the plot show the analytic prediction for events produced by wide-orbit planets. Similarly, the smooth cyan curves that start in the lower corners show the analytic prediction for events produced by close-orbit planets. The orange points show the times of events associated with caustic crossings. The full catalogue of simulation results is contained in appendix C.

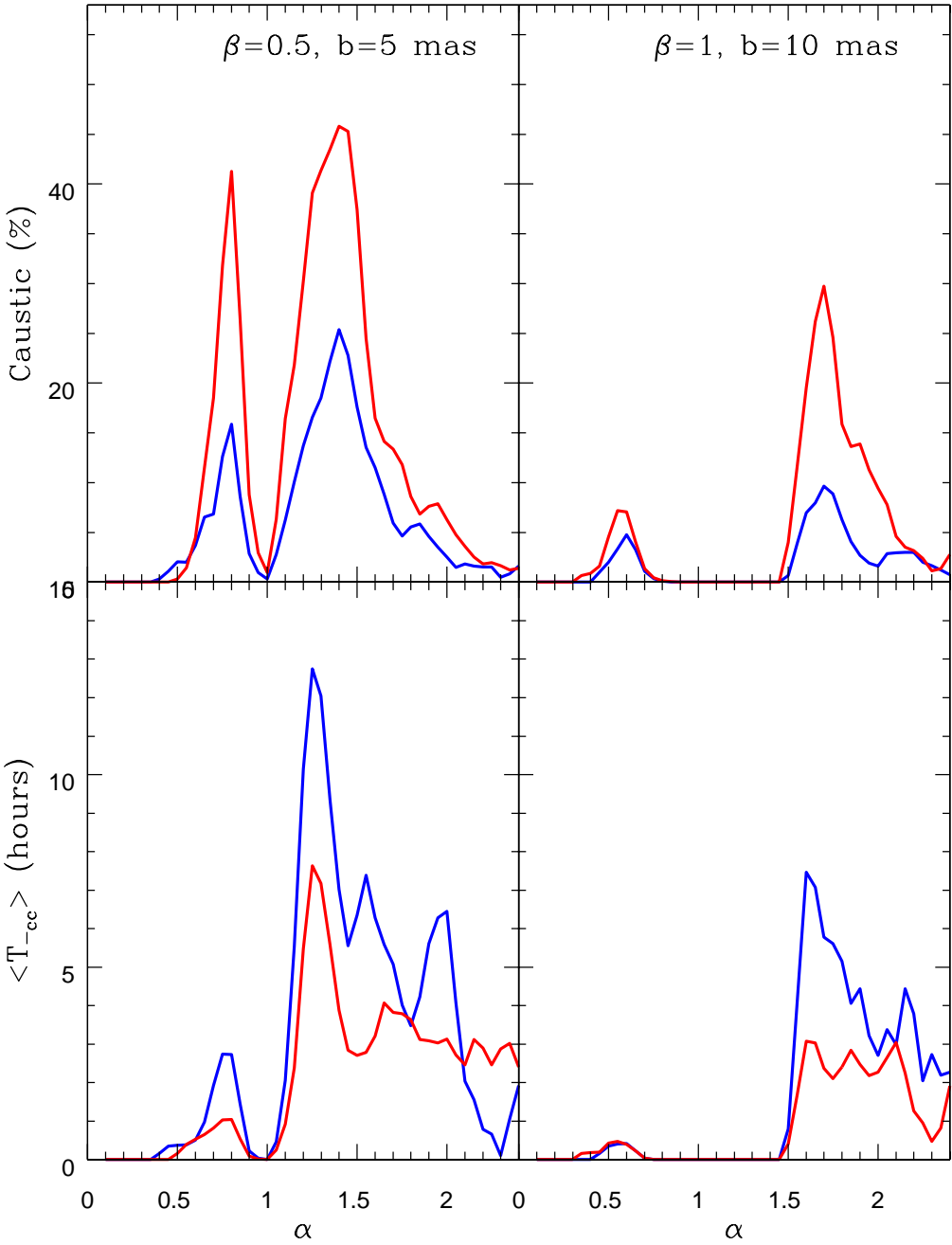


Figure 3.9: *Top:* Percentage of all light curves exhibiting caustics, versus α . *Bottom:* Average time between caustic crossings versus α . This graph was produced from the output of the simulations described in §3.3. The red and blue plots correspond to clockwise and counterclockwise respectively; the difference between them depends on which side of the source star is passed by the relative path of VB 10.

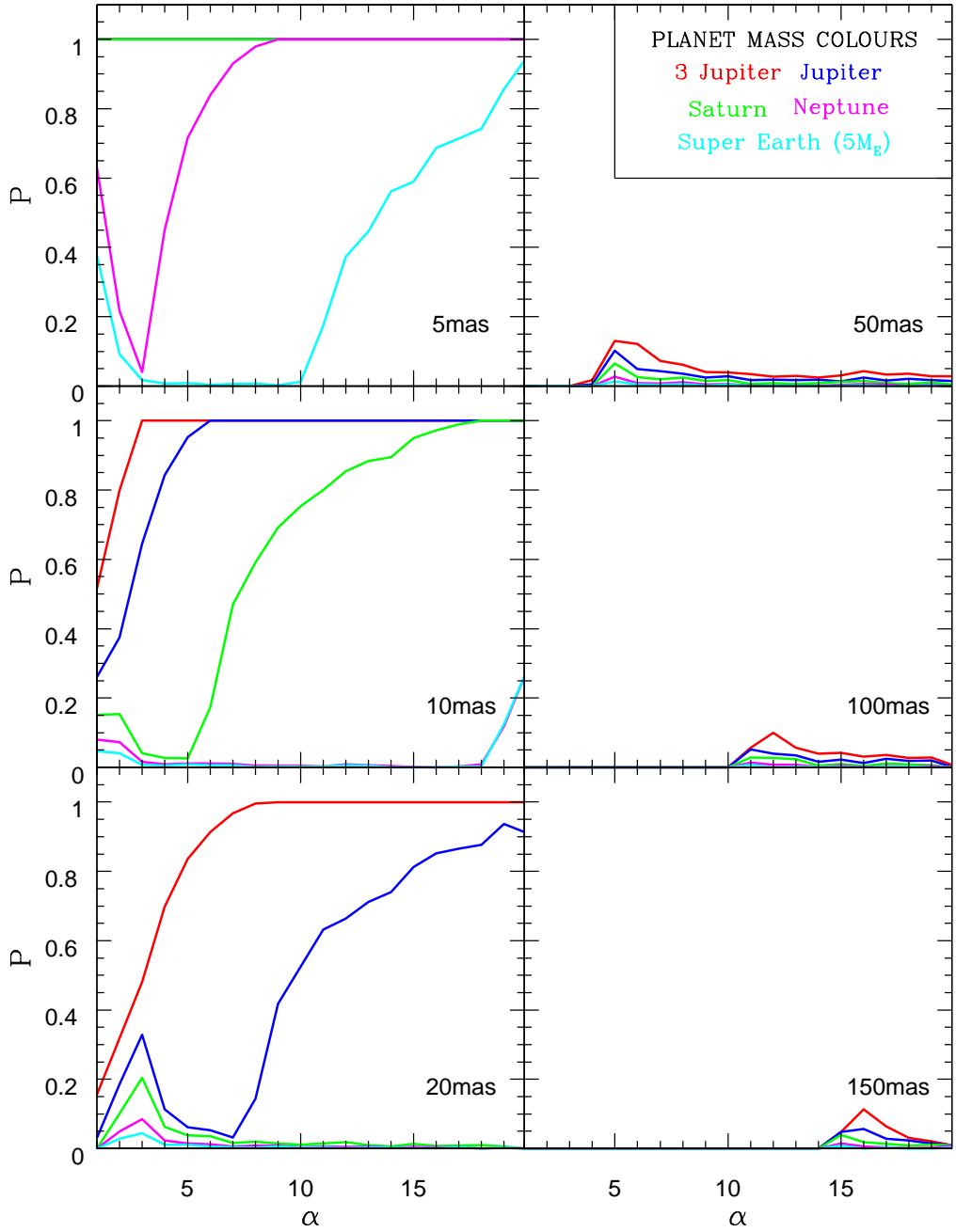


Figure 3.10: The probability of a planetary companion in the orbital range $\alpha \pm 0.5$ producing a deviation from single lens behaviour > 0.01 , as a function of α . This simulates 5 different mass ratios and the 6 different approaches described previously. The values of b are marked in each panel, and correspond to $\beta = 0.5, 1, 2, 5, 10$ and 15 .

3.5.1 Detection of Reflex Motion

As a planet orbits a star, it induces a ‘wobble’ in the stars orbit due to its gravitational influence; this is known as reflex motion. When u is small, for example due to close approaches, the induced motion in a star by a planetary companion can have a noticeable effect on the stellar-lens magnification, even if the lensing effect of the planet cannot be detected independently. This can be true for planets in all regimes, but is strongly dependent on β .

Figure 3.8 displays this effect prominently; many of the deviations produced very close to the time of closest approach are due to reflex motion in the star causing a deviation from its expected behaviour. This is exciting, as it potentially enables the discovery of planets with orbital parameters that would not otherwise enable detection through lensing. This effect is also responsible for the probabilities shown in figure 3.10; the massive planets cause the probability to tend to 1 for close approaches and wide orbits, as there will definitely be a deviation in magnification from a single lens on the path of the centre of mass. Figure 3.11 shows the maximum deviation from single lens behaviour caused by the reflex motion effect as a function of both α and β .

The effects of orbital motion on lensing in binary systems have been studied (Di Stefano 2012; Penny et al. 2011a; Penny et al. 2011b), but a full analysis of the prospects for planet hunting has not yet been carried out. Di Stefano et al. (2012a) contains a lengthier discussion.

3.5.2 The Effects of Orbital Orientation

From the derivation in §3.4.1 it is apparent that planets with certain values of Ω and i will be impossible to detect. Whilst most of the treatment for VB 10 has been conducted for face-on orbits, we have also carried out simulations where the values of Ω and i are varied. Figure 3.12 shows how orientation affects the time and approximate density of events for $\alpha = 5, \beta = 3$. As expected, there are ‘dead spots’ in orientation space- certain combinations of these two values where any planets in that particular configuration will be impossible to detect except by the reflex motion effect described above. This is an important factor to consider when analysing the prospects for planet detection, and would have to be taken into account when fitting the data to a theoretical model.

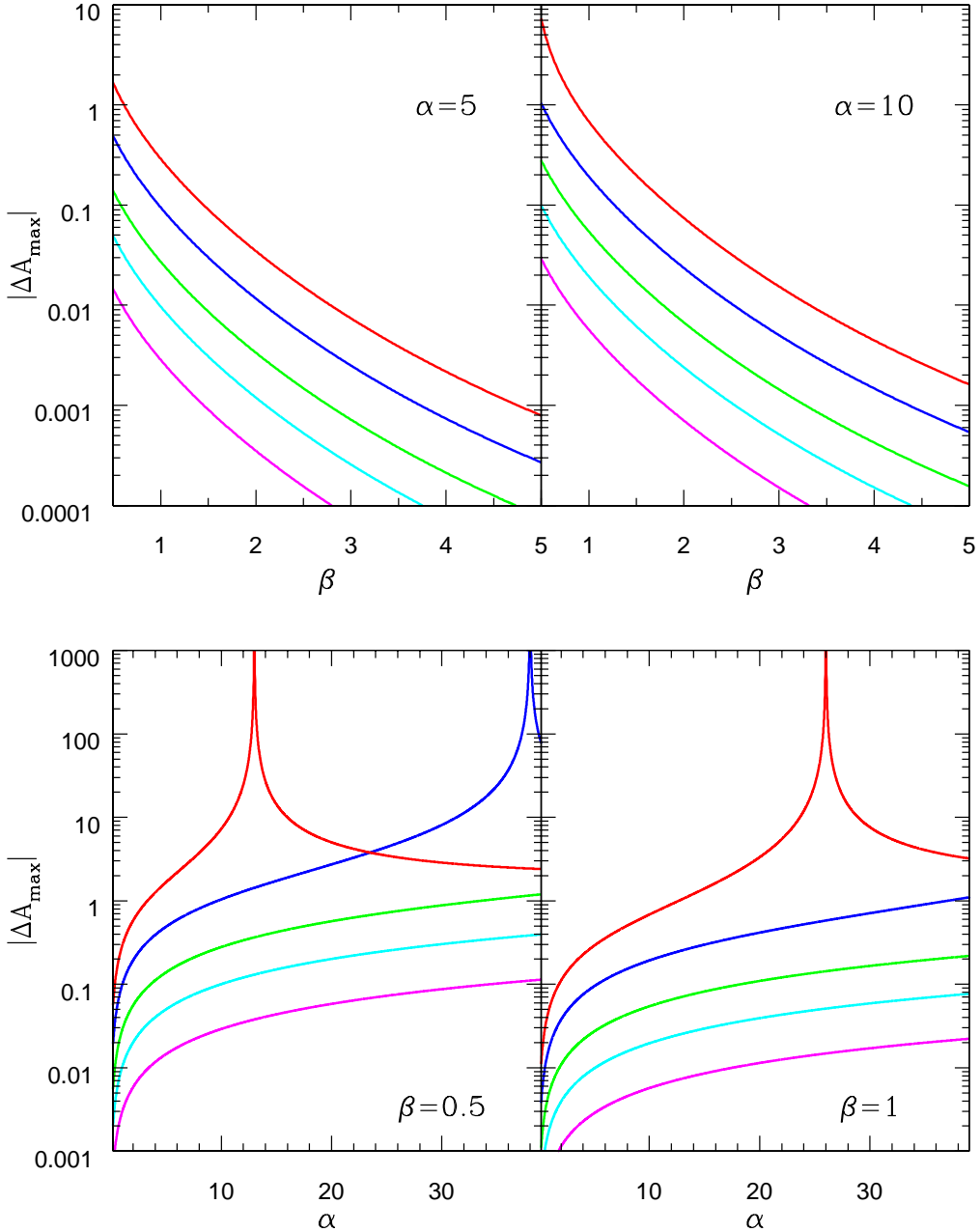


Figure 3.11: The maximum magnification difference from reflex motion, as a function of α and β . This example is for a $0.075M_{\odot}$ star, with 5 different values of q , the mass ratio shown in red, blue, green, cyan and magenta. These colours correspond to planet masses of 3 Jupiter, Jupiter, Saturn, Neptune and Super-Earth respectively, where a super-earth is defined as $m_p = 5m_{\oplus}$. The divergence in some of the curves is due to the reflex motion being strong enough to cause the lens to pass to the other side of the source star on the sky.

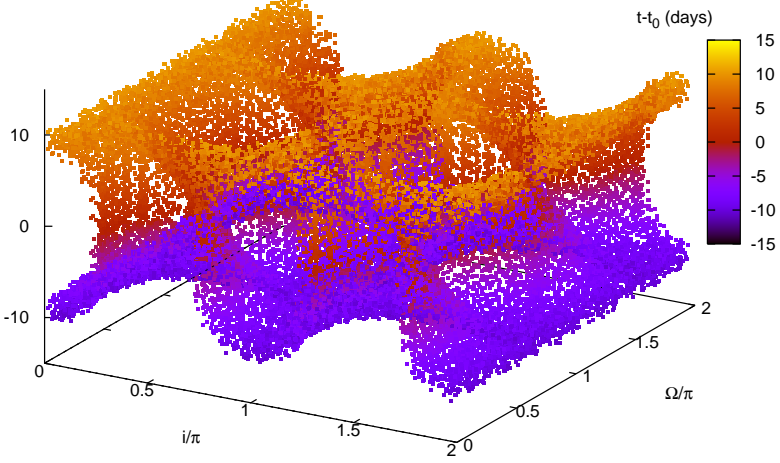


Figure 3.12: The effect of orientation and inclination on event times, for $\alpha = 5, \beta = 3$. The 3D plot shows $(t - t_0)$ as a function of Ω and i . ‘Dead spots’ occur when the orbit is close to edge-on and it is oriented such that the orbit can never pass close to the source on the sky, regardless of the starting phase. The colour of the points corresponds to the time either side of closest approach when the event occurs, and shows that orientation can have a profound effect on the timing of a planet-lens event.

3.6 Observations, Prospects and Future Work on the VB 10 Event

VB 10 has been observed by multiple members of the PLAN-IT team¹: Christopher Crockett (USNO), Jochen Greiner (GROND), Jake Turner (University of Arizona) and Zachory Berta (MEarth). Future work involves collection, calibration and analysis of these light curves, which will be carried out in the near future. The observing program is ongoing, but initial light curves from the MEarth and USNO observations can be seen in figure 3.13.

It should be stressed that there are severe limitations as to what we can learn about the VB 10 event at this time, due to a number of factors. First, the event is still ongoing, and so are the observations. Observation conditions were at their

¹http://www.cfa.harvard.edu/plan_it/

worst around December 2011, as is shown by the plot of solar angular distance in figure 3.4. These conditions improve throughout the spring and should continue to do so until observations cease in late May. We thus have a set of observations up to November 2011, and continuing from February 2012. In addition, the relative proper motion of VB 10 and [VB 10]-PMLS-1 is not yet properly constrained. This will be done in the near future, with scheduled Keck observations, in order to retrospectively analyse the data.

Whilst the chances of detecting planets may be small, there is still a great deal that can be learnt from this study. The foundations have been laid for the kind of network that would be needed to observe these events, which is known as the PLAN-IT program. Multi-waveband observations have been conducted at different longitudes in the style required for future events. Whilst we may find that no actual planet discoveries come from this study, once the proper motion is properly constrained it will be possible to place limits on further parameter spaces for planets. Most importantly, this has acted as a stepping-stone to future studies, and provides a useful case study for the first predicted mesolensing event to be studied in detail with the aim of finding exoplanets. An example of a process which is used to make future predictions is outlined in §4.3.1

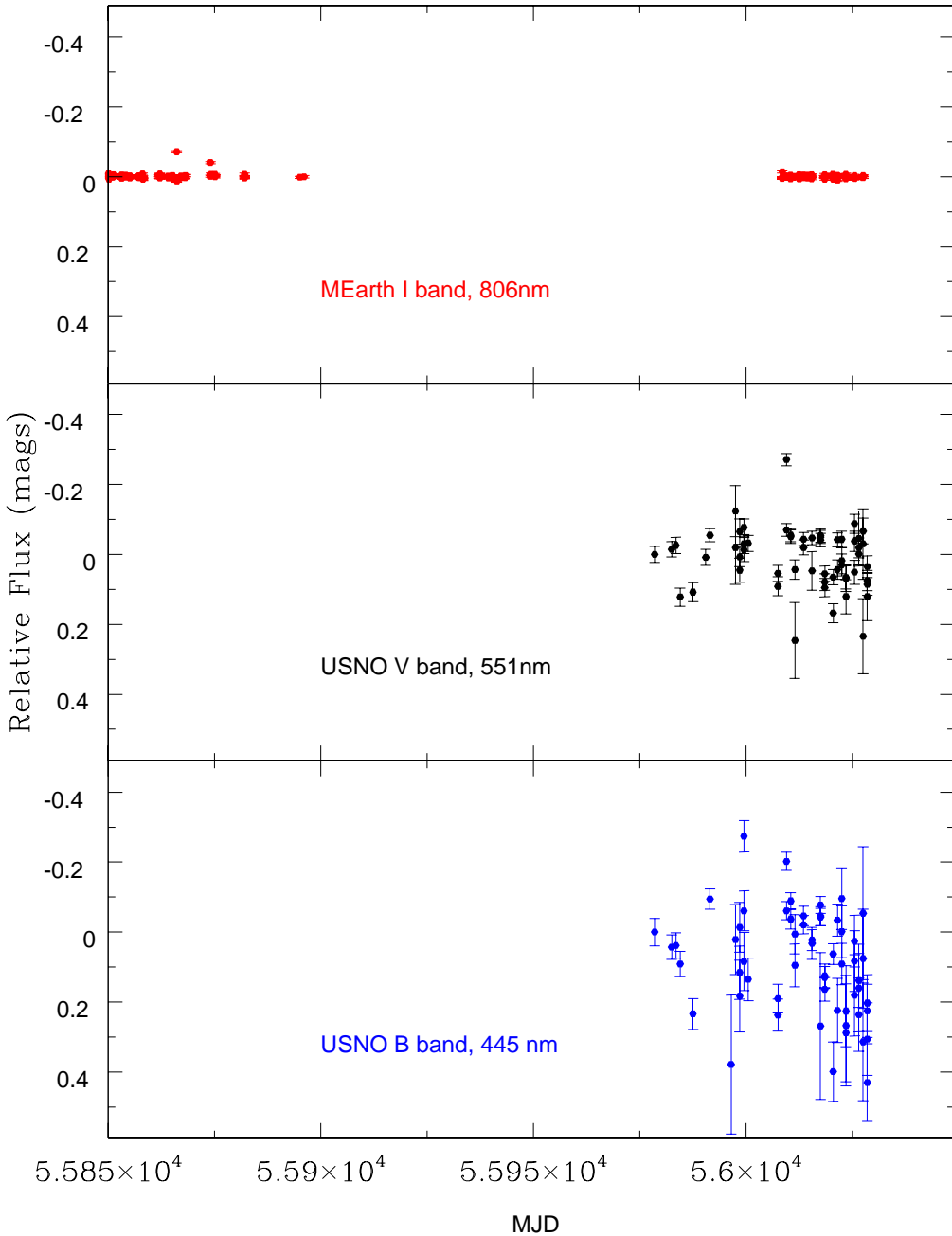


Figure 3.13: VB 10 light curve from USNO and MEarth observations, in I, B and V bands. This is intended as an illustration of the multi-waveband observation obtained, and the analysis of the data will take place in future months once the relative proper motions of the lens and source are constrained further. We would like to thank Christopher Crockett and Zachory Berta for the use of this data, and Jochen Greiner for his GROND observations.

Chapter 4

Predicting Future Events

4.1 Method and Catalogues

The next step in this study is to predict more mesolensing events. Predictions of mesolensing events have been made before (Salim & Gould 2000; Feibelman 1966), but until the VB 10 study none had considered the effects of planets or attempted to observe the predicted event. In addition, in the time since Salim and Gould's study new catalogues have become available, giving us deeper observations, more stars and more precise astrometric measurements. Feibelman's original prediction involving the 40 Eridani system turned out to be a near miss (Feibelman 1986), prompting him to remark:

“It is hoped that this 20-year exercise in frustration will encourage others to conduct systematic searches, perhaps by means of computer-based data banks, for stars with large proper motions that eventually may eclipse a background star and give rise to the elusive gravitational lens effect.”

This prophetic statement perhaps sums up best the methods we hope to employ, not only in the hope of learning about the lens stars, but also with the aim of discovering exoplanets. To predict lensing events in advance, we consider a nearby star (closer than ~ 500 pc) with known proper motion, which passes in front of a field of background stars with known positions. The key variables governing the likelihood of a lensing events are the Einstein angle, θ_E , the proper motion, μ , and the density of background stars, σ (see §4.2.2).

The Lépine-Shara Proper Motion (LSPM) catalogues (Lépine & Shara 2005a; Lépine et al. 2002; Lépine et al. 2003) are the current benchmark for catalogues of HPM stars. The LSPM catalogues are obtained using SUPERBLINK, an automated blink comparator (Lépine 2005), which can systematically analyse Digital

Sky Survey scans to obtain accurate proper motions (errors are typically around 8 mas). The published lists comprise 61,977 stars in the Northern sky (Lépine & Shara 2005b), and 2,228 stars in the south (Lépine 2008), with proper motions $\mu > 0.15''\text{yr}^{-1}$ and $\mu > 0.45''\text{yr}^{-1}$ in each case. In addition, we have access to more comprehensive lists down to $\mu = 0.04''\text{yr}^{-1}$ in the Northern sky ($\sim 1,100,000$ stars), and improved lists in the southern sky ($\sim 440,000$ stars).

To make predictions, the SUPERBLINK lists were used as a catalogue of candidate lenses, and an existing wide field survey catalogue as a list of sources. Some good candidate catalogues are available:

- The **Two Micron All Sky Survey (2MASS) Catalogue of Point Sources** is an all-sky catalogue of 470,992,970 sources. It contains photometric and astrometric information from epochs around the year 2000 for all of these sources. 2MASS has a relative astrometric accuracy in each field of ~ 20 mas (Lépine, private communication). Unfortunately, 2MASS only surveys in H, J and K bands, so it may be possible to miss some of the bluer background stars. One advantage of 2MASS is that the SUPERBLINK stars use 2MASS positions, so this eliminates the need for cross-catalogue correction and helps minimise the errors. 2MASS has a limiting J-band magnitude of $m_J = 17.1$ (Cutri et al. 2003b).
- The **USNO A2.0** catalogue¹ is an all sky catalogue of 526,280,881 stars. It contains positions and B and R magnitudes, obtained from reductions of Precision Measuring Machine plate scans from between 1950 and 1955. USNO A2.0 has a relative astrometric accuracy of ~ 200 mas (Assafin et al. 2001) and a limiting V-band magnitude² of $m_V \approx 20$.
- The **Panoramic Sky Telescope And Rapid-Response System (Pan-STARRS) 3π survey** (Kaiser et al. 2002) covers a large portion of the sky with good relative astrometric accuracy (estimated to be as low as ~ 1 mas; Chambers 2005). The Pan-STARRS 3π survey is recent- epochs can be as recent as 2010. The catalogues of Pan-STARRS point sources are available on the Harvard FAS Odyssey Cluster, and are estimated to be complete to limiting magnitudes³ in I and G of $m_I \approx 23.9, m_G \approx 24.6$. This is a considerable improvement on USNO A2.0 and 2MASS.

In this study we have used Pan-STARRS data to assess the mesolensing event rate in the *Kepler* field. This is because it is complete to lower magnitudes than the other catalogues, which is crucial in such a small area of the sky. We have

¹<http://tdc-www.harvard.edu/catalogs/ua2.html>

²<http://www.brightastro.org/asteroids/USNO%20photometry.htm>

³Pan-STARRS PS1 Mission Concept Statement: <http://www.ifa.hawaii.edu/users/chambers/ps1sc/documents/MissionConceptStatement.pdf>

not yet predicted individual events with Pan-STARRS, but we have analysed the prospects for using the SUPERBLINK stars in the *Kepler* field as an ensemble of mesolenses. 2MASS has been used as a catalogue for all-sky predictions, and a specific prediction involving the low mass M dwarf GJ1214 has been made.

One major problem with using recent catalogues (such as 2MASS and Pan-STARRS) is that around each lens star there is an effective ‘blind spot’. The relative brightness of the nearby HPM star creates a zone of exclusion within $\sim 5''$, as it is harder to see a dim star. This was noticed by observing a density gradient in background sources as distance from the lens star increased. This is obviously problematic for the lower proper motion stars in the SUPERBLINK lists; a star with $\mu = 0.1''\text{yr}^{-1}$ would take around half a century to move out of this blind spot in the catalogues. Fortunately, using older catalogues such as USNO A2.0 (with its 1950–1955 epoch) means that most stars will have moved out of this zone of exclusion, and will be passing over a region whose background density in the catalogue is not affected by this problem.

4.2 Lensing in the Kepler Field

The *Kepler* space mission is designed to find exoplanets using the transit method and has had great success (see §1; Borucki et al. 2010; Borucki et al. 2011). 7474 of the HPM stars in the SUPERBLINK lists lie in the *Kepler* field. Figure 4.1 shows the locations of these stars, colour-coded according to the nearby background density. A strong density gradient exists across the field, which can affect the probability of lensing in a given *Kepler* chip.

4.2.1 Why Kepler?

There are a number of reasons for focusing on the *Kepler* field. The first and most advantageous aspect is that *Kepler* is capable of exquisite millimagnitude photometry (Koch et al. 2010), making it an exciting tool for discovering planets through lensing, in addition to the mission goal. Thus, *Kepler* is sensitive to the close-orbit planet effects described in §2.3.1 and §3.4.2.

Although our primary long term goal is to predict future events, it is also possible to utilise past surveys to identify lensing events retrospectively. One advantage of the *Kepler* field is that it has been analysed by the ‘Digital Access to a Sky Century @ Harvard’ (DASCH) survey (Tang et al. 2011) as part of their digitisation of the all-sky Harvard plate stacks. The DASCH survey analyses $\sim 500,000$ photographic plates for both astrometric and photometric information. The plates have $\sim 500 - 1,000$ images of every point on the sky obtained between 1880 and 1985 (Laycock et al. 2008). This unprecedented timescale dramatically impacts on the

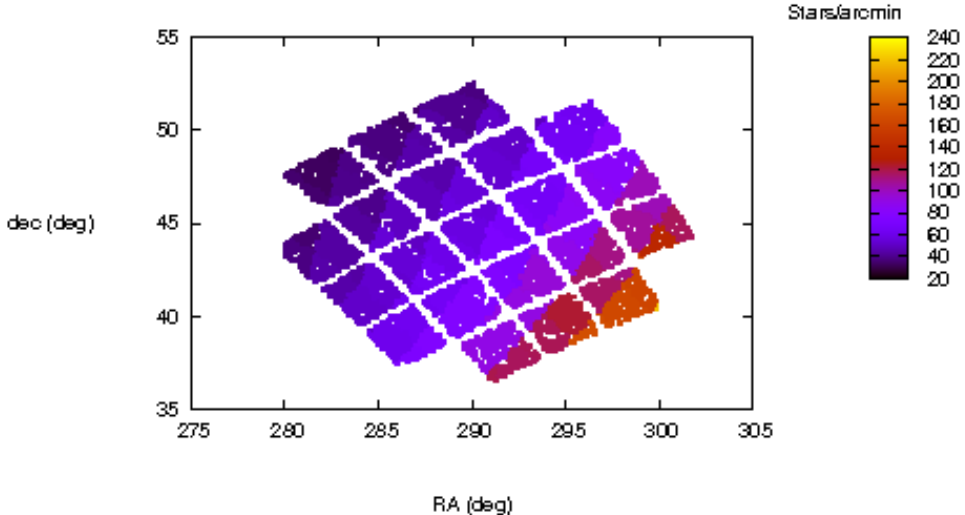


Figure 4.1: Points marking the SUPERBLINK stars in the *Kepler* field, with the colour of the point corresponding to the number of stars per arcminute within a degree of the HPM star. The patchwork appearance is due to the layout of the *Kepler* chips.

integrated probability of seeing lensing events. By applying the same logic we use to predict events, we can also extrapolate proper motions backwards in time to discover where we would expect DASCH lensing events to occur. The database can then be checked for variability around the location and time calculated.

4.2.2 The Mesolensing Event Rate

It is possible to estimate the number of events the lenses in the SUPERBLINK *Kepler* sample will produce per year. The key quantity when considering the rate of mesolensing events is the area, A_{meso} , swept out per year by the Einstein diameter of a lens:

$$A_{meso} = 2\theta_E \mu \quad (4.1)$$

If we define an event as any approach where $\beta \leq \beta_{ev}$ then the relevant area to consider is $\beta_{ev}A_{meso}$. The event rate R for an ensemble of n lenses is therefore given by

$$R = \sum_{i=1}^n \beta_{ev} \sigma_i A_{meso,i} = \sum_{i=1}^n 2\sigma_i \beta_{ev} \theta_{E,i} \mu_i \quad (4.2)$$

where σ_i is the background star density on the sky around a particular lens. Whilst this quantity can be estimated by assuming a typical value for θ_E and μ , we can make a better estimate by considering each lens individually (as in equation 4.2). This can be done by using mass and distance estimates (with varying degrees of reliability) to calculate θ_E for the candidate lens and using equation 4.2. The background density of stars σ_i comes from the density around each star in the catalogue as shown in figure 4.1. The total rates for a few interesting values of β_{ev} are shown in table 4.1, and a histogram of the rates for each star is shown in figure 4.2. We will define a ‘detectable stellar event’ as any event with $\beta \leq 3.5$, as when $u = 3.5$ the magnification is approximately 1%. $\beta_{ev} = 100$ is an approximate maximum value for detecting wide-orbit planets, although the precise boundary that is appropriate depends on the physical dimensions involved and should be assessed individually in each case.

Catalogue	$R(\beta_{ev} = 1)\text{yr}^{-1}$	$R(\beta_{ev} = 3.5)\text{yr}^{-1}$	$R(\beta_{ev} = 100)\text{yr}^{-1}$
2MASS	0.013	0.045	1.31
USNO A2.0	0.021	0.074	2.14
Pan-STARRS	0.080	0.28	8.02

Table 4.1: Event rates with various catalogues for the SUPERBLINK stars.

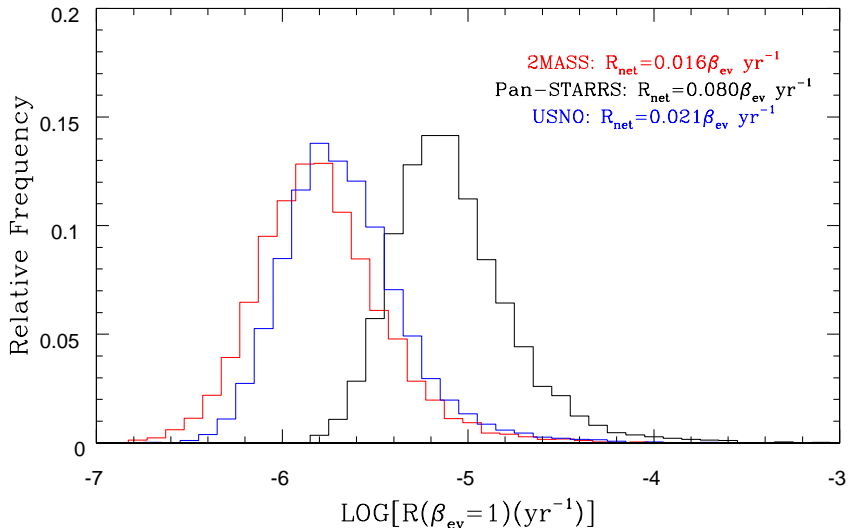


Figure 4.2: A histogram showing the logarithm to base 10 of event rates for the SUPERBLINK stars inside the *Kepler* field with various catalogues. The total rates are also marked. Pan-STARRS producing a notably higher event rate, due to a higher completeness and background density.

4.3 2MASS Predictions

The CDS X-match tool⁴ was used to find nearby 2MASS stars to the SUPERBLINK candidate lenses, and the FORTRAN code *2mass_match* was then used to extrapolate proper motion and record approaches with $\beta \leq 100$. We are still assessing the reliability of our all-sky results, and will present them in future months. However, we were able to make a prediction involving the nearby star GJ1214. We decided to study this further, as *HST* observations were available, which enable the errors associated with the event to be minimised.

4.3.1 GJ1214

GJ1214, like VB 10, is a low-mass ($0.16M_{\odot}$) M dwarf, with a K-band magnitude of $m_K = 8.80$ (Cutri et al. 2003a). It is a MEarth target star, and was recently found to have a planetary companion, GJ1214b. MEarth observed a planetary transit (Charbonneau et al. 2009). Follow up work characterised the planet as a $6.6m_{\oplus}$ ‘waterworld’ with an orbital period of about 1.58 days (Miller-Ricci & Fortney 2010; Berta et al. 2011). As it happens, GJ1214 has an Einstein angle very similar to VB 10, with $\theta_E \approx 10$ mas.

GJ1214 has a relative proper motion of $0.948''\text{yr}^{-1}$ (Lépine & Shara 2005b). By simulating GJ1214’s motion and recording angular distances to its nearby background stars, we have found that it makes an approach of $b \approx 443$ mas ($\beta \approx 44.3$) to a nearby background star in the year 2025. For the purposes of this case study we shall call this background star [GJ1214]-PMLS-1, consistent with the convention for VB 10. [GJ1214]-PMLS-1 (2MASS number 17151993+0457312) has apparent magnitudes in J,H and K bands of approximately 14.8, 15.6 and 14.3 respectively (according to 2MASS).

The Prediction and Associated Challenges

Including an error analysis from a Monte Carlo simulation which uses constraints from *HST* images (see §4.3.1, *Errors and Uncertainties*), it is possible to predict an event with the characteristics shown in table 4.2.

From equation 3.1 it is apparent that the blended magnitude in J band without lensing would be 9.74, and a 10% magnification would cause a 0.001 change in magnitude. Although this is challenging, millimagnitude photometry has already been achieved on this specific star in the GJ1214b discovery paper (Charbonneau et al. 2009), so an event of this magnitude could potentially be detectable. Furthermore, GJ1214 is much dimmer in bluer bands. It has V and B band magnitudes of $m_V = 14.71$ and $m_B = 16.72$ (Berta et al. 2011; Monet et al. 2003). From the

⁴<http://cdsxmatch.u-strasbg.fr/xmatch>

Parameter	Value	$\sigma_{err}(\pm)$
b (mas)	443	161
β (b/θ_E)	44.3	16.1
t_0	29 Sep. 2025	62.1 days
RA ₀ (deg)	258.833034	3.68×10^{-5}
dec ₀ (deg)	4.958596	2.90×10^{-5}

Magnitude	GJ1214	[GJ1214]-PMLS-1
m_K	8.80	14.3
m_H	9.09	15.6
m_J	9.75	14.8
m_V	14.71	≈ 17.7
m_B	16.72	Unknown

Table 4.2: Characteristics of the GJ1214 event. m_X is the apparent magnitude in band X, obtained with 2MASS magnitudes. t_0 is the time of closest approach, and (RA₀, dec₀) is the position of the lens at closest approach.

V-band images taken by Berta et al. (with the KeplerCam on the Fred Lawrence Whipple Observatory 1.2 m telescope) we were able to estimate the V-band magnitude of [GJ1214]-PMLS-1 at $m_V \approx 17.7$. In this case a 10% magnification would cause a 0.007 change in magnitude from an original V-band blended magnitude of 14.64. It is therefore apparent that V-band may be more suited to observations than redder bands due to the lower magnitude of GJ1214 at this wavelength.

The value of β for this event places us firmly in the wide regime, meaning we are reliant on an independent planet-lens event. We could potentially be sensitive to planets with $\alpha \gtrsim 38$ which corresponds to a physical separation of $a \gtrsim 4.9$ AU. From equation 3.4 we find there is a probability of $\sim 0.7\%$ that a planet of $\alpha = 50$ would produce a 1% deviation for $\beta = 44.3$. Whilst the probability of detecting planets with this specific event may be low, it shows that by combining the method outlined previously with analysis of images with higher astometric precision than the catalogue it is possible to make predictions with reasonable associated uncertainties.

If we can monitor hundreds, or thousands, of stars which are expected to produce events then the probability of detecting a planet in a given timescale is dramatically increased. This could be done in a similar way to the MEarth survey, which monitors 2089 stars in the hope of observing transiting planets. A MEarth-like survey, operating in multiple wavebands, could therefore have good chances of discovering by monitoring ensembles of candidates mesolenses.

Errors and Uncertainties

To improve the errors from those in 2MASS, we studied *HST* images of the field around GJ1214 (shown in figure 4.3). This provided a position on 23 July 2011 (MJD 55765.0), reducing the error in propagating the proper motion errors of 8 mas. A Monte Carlo simulation was then conducted. We calculated the initial positions of the lens and source from a Gaussian with a standard deviation of $\sigma_{err} = 0.08''$ (from the *HST* images) and chose its proper motion similarly with $\sigma_{err} = 0.008''$. The proper motion of the background star could be constrained to $\lesssim 0.01''\text{yr}^{-1}$ using the *HST* epochs, so the proper motion was similarly chosen from a Gaussian with $\sigma_{err} = 0.01''$ in this case.

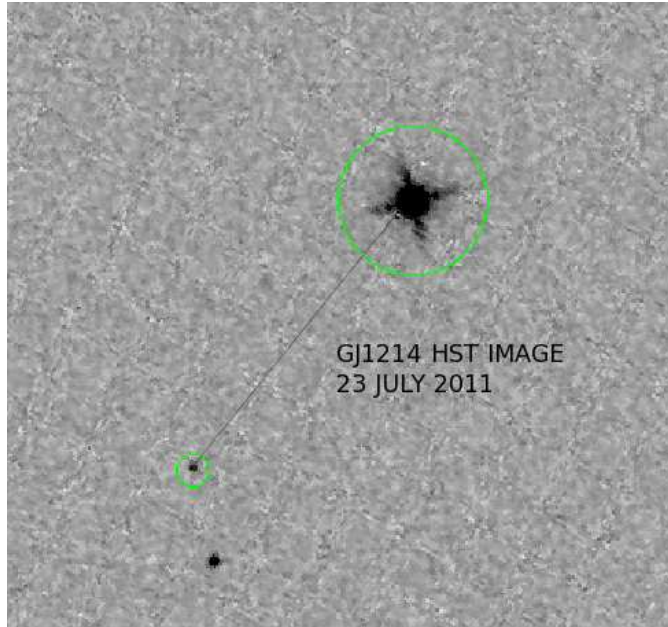


Figure 4.3: *HST* image taken on 23 July 2011 of the field around GJ1214. GJ1214 and [GJ1214]-PMLS-1 are identified with green circles, and the relative proper motion direction is shown with a line. Two nearby background stars close to GJ1214 can be clearly seen in the bottom left corner of the image. [GJ1214]-PMLS-1 is the fainter of the two.

4.4 Overall Prospects and Future Work

The prediction of the GJ1214 event shows that making predictions using catalogues is possible, and that, as with VB 10, refining the prediction with *HST* images

helps to minimise the uncertainties. Future work on making predictions should be concentrated in a few key areas:

- The 2MASS catalogue and USNO A2.0 catalogues should be utilised to make whole sky predictions. USNO A2.0 can be used for short-term predictions and predictions involving lower proper motion stars, whilst the 2MASS catalogue can be utilised in the same way as described in §4.3.
- A specific study of the GJ1214 event should be undertaken in the same manner as the VB 10 study. The timing of the event means that it is possible to further constrain the proper motion of both the lens and source. Future *HST* or Keck Adaptive Optics (AO) observations should be taken of the field around GJ1214 closer to the event, in a procedure which can also be applied to the general case of predicted events.
- The potentials of other catalogues of lens candidates should be explored. Some examples would be catalogues of White Dwarfs such as those produced by Harris et al. (2006) and Sion et al. (2009).
- The Pan-STARRS 3π survey data should be utilised to make specific predictions in the *Kepler* field and also across the whole sky. K-d tree routines in Python (nearest neighbour algorithms for k-dimensional space; Bentley 1975) can be utilised when studying this data to speed up the process.
- The Harvard plate stacks that have been analysed by DASCH should be checked for evidence of lensing, and the process outlined to predict future events can be used to retrospectively analyse the data for lensing events.

Chapter 5

Conclusion

The in depth study of the VB 10 lensing event presented here (§3) and in Di Stefano et al. (2012a; 2012b) laid the foundations for a broader understanding of the prospects for exoplanet discovery using predicted mesolensing events. It is hoped that the broader swathe of mesolensing studies, of which this work forms part, will ascertain what might be possible to discover with this method. Whilst the prospects for planet discovery are not as good as one might hope, specific mesolensing surveys could make significant discoveries, perhaps in symbiosis with other science. It is also suggested the data from existing microlensing surveys is assessed in an attempt to discover planets in each of the three regimes discussed. Specifically, we can draw a number of important conclusions from our study.

The lensing signatures presented here confirm that, with observations that have individually tailored cadence and photometry, it is possible to detect planets at almost all orbital separations with mesolensing. The combination of the close regime (Di Stefano 2011), wide regime (Di Stefano & Scalzo 1999) and the resonant regime traditionally studied with microlensing creates a parameter space extending from $\alpha \sim 0.1$ right out to the widest orbits. Although the observational capabilities required to observe effects and the probabilities associated with an event occurring are very different, the sensitivity to each regime can be assessed in each case. Lensing studies should develop data pipelines to search for all types of effects, and the *Kepler* data taken so far should be analysed (this work has already been started by our team).

We have analysed the predicted VB 10 event in depth, and conducted detailed simulations in all three orbital regimes. These simulations have shown the probability of a potentially detectable event depends strongly on three main variables: α , q and β . On top of this, there are observational difficulties relating to the magnitudes and positions on the sky of the lens and source, and the consideration of the timescale of planetary events in comparison to the cadence of the observing instrument. All in all, the chances of detecting a planet during the event appear to

be small, but the potential scientific value of a discovery would be great. We can also learn interesting information about VB 10 itself (e.g. mass measurement) from the observations required to discover planets. Limited preliminary data from the PLAN-IT observing teams has been obtained, as the event is potentially still ongoing. Importantly, the multi-waveband observations required have been taken, serving as a useful learning exercise for future predictions. The VB 10 event shows that predicting mesolensing events is a feasible way to enhance the chances of detecting planets. Although the probabilities associated with individual events may be small, by monitoring ensembles of events at a relatively low observational cost we will be able to make regular, if infrequent discoveries. It will also be possible to continuously place limits on the possible parameter space exoplanets around nearby stars can occupy.

We have assessed the mesolensing event rates in the *Kepler* field, using this example to illustrate the all-sky prospects. It has been estimated that the SUPERBLINK stars in the *Kepler* field will produce ~ 0.24 detectable events per year with close approaches to Pan-STARRS sources. The number of approaches potentially close enough to potentially detect planets is expected to be ~ 8 per year.

Finally, the catalogue-matching methods outlined in §4 have been used to predict a specific event involving the nearby M-dwarf GJ1214, which hosts a planetary companion. The event is predicted to have an angular distance of closest approach of $b = 443 \pm 161$ mas and a time of closest approach of 29 September 2025 (± 62.1 days). A brief discussion of the prospects for discovering more about the GJ1214 system from this event has been undertaken. It is hoped successful *HST* observations closer to the time of the event can help constrain the parameters of this prediction as well as similar future predictions.

There is a scope for future work in this area along a number of different avenues, some of which have been identified in §3.6 and §4.4. It is hoped that a natural progression from the work here will mean that in the future it will be possible to produce a ‘calendar’ of mesolensing events, with viable prospects of discovering nearby planets in a systematic manner.

Acknowledgements

I would like to thank Rosanne Di Stefano for supervising and directing this work, and being a supportive and enthusiastic supervisor throughout. I would like to thank and acknowledge Shude Mao for the development of the original binary lens code. The event prediction procedures were run on the *Odyssey* cluster supported by the FAS Science Division Research Computing Group at Harvard University, and the 2MASS and USNO A2.0 data were obtained using the ViZier CDS X-

match service. I acknowledge the use of the 2MASS catalogue of point sources, the USNO A2.0 catalogue and the Pan-STARRS 3π survey. Pavlos Protopapas was immensely helpful in utilising the Pan-STARRS data.

I would like to thank all the PLAN-IT contributors for the use of their data, and for their support and advice throughout: Jochen Greiner, Jake Turner, Christopher Crockett, Allyn Smith, Sébastien Lépine, Zachory Berta, Fred Walter and John Johnson. I am especially grateful to Zachory Berta for his help regarding MEarth and GJ1214, and Sébastien Lépine for his invaluable expertise concerning high proper motion stars. I also acknowledge the use of Sébastien's SUPERBLINK catalogues.

Finally, I would like to thank Malcolm Coe, Phil Charles and Mike Garcia for organising the year abroad at the CfA, and am eternally grateful to Sam Connolly, Poppy Martin and Ruth Angus for advice and friendship.

Bibliography

- Anglada-Escudé G., Arriagada P., Vogt S. S., Rivera E. J., Butler R. P., Crane J. D., Shectman S. A., Thompson I. B., Minniti D., Haghhighipour N., Carter B. D., Tinney C. G., Wittenmyer R. A., Bailey J. A., O'Toole S. J., Jones H. R. A., Jenkins J. S., 2012, ArXiv:1202.0446
- Anglada-Escudé G., Shkolnik E. L., Weinberger A. J., Thompson I. B., Osip D. J., Debes J. H., 2010, ApJ Letters, 711, L24
- Assafin M., Andrei A. H., Martins R. V., da Silva Neto D. N., Camargo J. I. B., Teixeira R., Benevides-Soares P., 2001, ApJ, 552, 380
- Ballard S., Fabrycky D., Fressin F., Charbonneau D., Desert J.-M., Torres G., Marcy G., Burke C. J., Isaacson H., Henze C., Steffen J. H., Ciardi D. R., Howell S. B., Cochran W. D., Endl M., Bryson S. T., Rowe J. F., Holman M. J., Lissauer J. J., Jenkins J. M., Still M., Ford E. B., Christiansen J. L., Middour C. K., Haas M. R., Li J., Hall J. R., McCauliff S., Batalha N. M., Koch D. G., Borucki W. J., 2011, ApJ, 743, 200
- Batista V., Gould A., Dieters S., Dong S., Bond I., Beaulieu J. P., Maoz D., Monard B., Christie G. W., McCormick J., Albrow M. D., Horne K., Tsapras Y., Burgdorf M. J., Calchi Novati S., Skottfelt J., Caldwell J., Kozłowski S., Kubas D., Gaudi B. S., Han C., Bennett D. P., An J., The MOA Collaboration, Abe F., Botzler C. S., Douchin D., Freeman M., Fukui A., Furusawa K., Hearnshaw J. B., Hosaka S., Itow Y., Kamiya K., Kilmartin P. M., Korpela A., Lin W., Ling C. H., Makita B. S., Masuda K., Matsubara Y., Miyake N., Muraki Y., Nagaya M., Nishimoto K., Ohnishi K., Okumura T., Perrott Y. C., Rattenbury N., Saito T., Sullivan D. J., Sumi T., Sweatman W. L., Tristram P. J., von Seggern E., Yock P. C. M., The PLANET Collaboration, Brilliant S., Calitz J. J., Cassan A., Cole A., Cook K., Coutures C., Dominis Prester D., Donatowicz J., Greenhill J., Hoffman M., Jablonski F., Kane S. R., Kains N., Marquette J.-B., Martin R., Martioli E., Meintjes P., Menzies J., Pedretti E., Pollard K., Sahu K. C., Vinter C., Wambsganss J., Watson R., Williams A., Zub M., The FUN Collaboration, Allen W., Bolt G., Bos M., DePoy D. L., Drummond J., Eastman J. D., Gal-Yam A., Gorbikov E., Higgins D., Janczak

J., Kaspi S., Lee C.-U., Mallia F., Maury A., Monard L. A. G., Moorhouse D., Morgan N., Natusch T., Ofek E. O., Park B.-G., Pogge R. W., Polishook D., Santallo R., Shporer A., Spector O., Thornley G., Yee J. C., The MiNDSTEp Consortium, Bozza V., Browne P., Dominik M., Dreizler S., Finet F., Glitstrup M., Grundahl F., Harpsøe K., Hessman F. V., Hinse T. C., Hundertmark M., Jørgensen U. G., Liebig C., Maier G., Mancini L., Mathiasen M., Rahvar S., Ricci D., Scarpetta G., Southworth J., Surdej J., Zimmer F., The RoboNet Collaboration, Allan A., Bramich D. M., Snodgrass C., Steele I. A., Street R. A., 2011, *A&A*, 529, A102

Bean J. L., Seifahrt A., Hartman H., Nilsson H., Reiners A., Dreizler S., Henry T. J., Wiedemann G., 2010, *ApJ Letters*, 711, L19

Bentley J. L., 1975, *Communications of the ACM*, 18, 509

Berger E., Basri G., Gizens J. E., Giampapa M. S., Rutledge R. E., Liebert J., Martín E., Fleming T. A., Johns-Krull C. M., Phan-Bao N., Sherry W. H., 2008, *ApJ*, 676, 1307

Berta Z. K., Charbonneau D., Bean J., Irwin J., Burke C. J., Désert J.-M., Nutzman P., Falco E. E., 2011, *ApJ*, 736, 12

Borucki W. J., Koch D., Basri G., Batalha N., Brown T., Caldwell D., Caldwell J., Christensen-Dalsgaard J., Cochran W. D., DeVore E., Dunham E. W., Dupree A. K., Gautier T. N., Geary J. C., Gilliland R., Gould A., Howell S. B., Jenkins J. M., Kondo Y., Latham D. W., Marcy G. W., Meibom S., Kjeldsen H., Lissauer J. J., Monet D. G., Morrison D., Sasselov D., Tarter J., Boss A., Brownlee D., Owen T., Buzasi D., Charbonneau D., Doyle L., Fortney J., Ford E. B., Holman M. J., Seager S., Steffen J. H., Welsh W. F., Rowe J., Anderson H., Buchhave L., Ciardi D., Walkowicz L., Sherry W., Horch E., Isaacson H., Everett M. E., Fischer D., Torres G., Johnson J. A., Endl M., MacQueen P., Bryson S. T., Dotson J., Haas M., Kolodziejczak J., Van Cleve J., Chandrasekaran H., Twicken J. D., Quintana E. V., Clarke B. D., Allen C., Li J., Wu H., Tenenbaum P., Verner E., Bruhwiler F., Barnes J., Prsa A., 2010, *Science*, 327, 977

Borucki W. J., Koch D. G., Basri G., Batalha N., Brown T. M., Bryson S. T., Caldwell D., Christensen-Dalsgaard J., Cochran W. D., DeVore E., Dunham E. W., Gautier III T. N., Geary J. C., Gilliland R., Gould A., Howell S. B., Jenkins J. M., Latham D. W., Lissauer J. J., Marcy G. W., Rowe J., Sasselov D., Boss A., Charbonneau D., Ciardi D., Doyle L., Dupree A. K., Ford E. B., Fortney J., Holman M. J., Seager S., Steffen J. H., Tarter J., Welsh W. F., Allen C., Buchhave L. A., Christiansen J. L., Clarke B. D., Das S., Désert J.-M., Endl M., Fabrycky D., Fressin F., Haas M., Horch E., Howard A., Isaacson

H., Kjeldsen H., Kolodziejczak J., Kulesa C., Li J., Lucas P. W., Machalek P., McCarthy D., MacQueen P., Meibom S., Miquel T., Prsa A., Quinn S. N., Quintana E. V., Ragozzine D., Sherry W., Shporer A., Tenenbaum P., Torres G., Twicken J. D., Van Cleve J., Walkowicz L., Witteborn F. C., Still M., 2011, ApJ, 736, 19

Borucki W. J., Koch D. G., Batalha N., Bryson S. T., Rowe J., Fressin F., Torres G., Caldwell D. A., Christensen-Dalsgaard J., Cochran W. D., DeVore E., Gautier T. N., Geary J. C., Gilliland R., Gould A., Howell S. B., Jenkins J. M., Latham D. W., Lissauer J. J., Marcy G. W., Sasselov D., Boss A., Charbonneau D., Ciardi D., Kaltenegger L., Doyle L., Dupree A. K., Ford E. B., Fortney J., Holman M. J., Steffen J. H., Mullally F., Still M., Tarter J., Ballard S., Buchhave L. A., Carter J., Christiansen J. L., Demory B.-O., Désert J.-M., Dressing C., Endl M., Fabrycky D., Fischer D., Haas M. R., Henze C., Horch E., Howard A. W., Isaacson H., Kjeldsen H., Johnson J. A., Klaus T., Kolodziejczak J., Barclay T., Li J., Meibom S., Prsa A., Quinn S. N., Quintana E. V., Robertson P., Sherry W., Shporer A., Tenenbaum P., Thompson S. E., Twicken J. D., Van Cleve J., Welsh W. F., Basu S., Chaplin W., Miglio A., Kawaler S. D., Arentoft T., Stello D., Metcalfe T. S., Verner G. A., Karoff C., Lundkvist M., Lund M. N., Handberg R., Elsworth Y., Hekker S., Huber D., Bedding T. R., Rapin W., 2012, ApJ, 745, 120

Cassen P., 2006, in D. Queloz, S. Udry, M. Mayor, W. Benz, P. Cassen, T. Guillot, & A. Quirrenbach (ed.), Saas-Fee Advanced Course 31: Extrasolar planets, p. 369

Chabrier G., Baraffe I., Allard F., Hauschildt P., 2000, ApJ, 542, 464

Chambers K. C., 2005, in P. K. Seidelmann & A. K. B. Monet (ed.), Astrometry in the Age of the Next Generation of Large Telescopes, Vol. 338 of *Astronomical Society of the Pacific Conference Series*, 134

Charbonneau D., Berta Z. K., Irwin J., Burke C. J., Nutzman P., Buchhave L. A., Lovis C., Bonfils X., Latham D. W., Udry S., Murray-Clay R. A., Holman M. J., Falco E. E., Winn J. N., Queloz D., Pepe F., Mayor M., Delfosse X., Forveille T., 2009, Nature, 462, 891

Cutri R., Skrutskie M., Van Dyk S., Beichman C., Carpenter J., Chester T., Cambresy L., Evans T., Fowler J., Gizis J., Howard E., Huchra J., Jarrett T., Kopan E., Kirkpatrick J., Light R., Marsh K., McCallon H., Schneider S., Stiening R., Sykes M., Weinberg M., Wheaton W., Wheelock S., Zacharias N., 2003b, Explanatory Supplement to the 2MASS All Sky Data Release, <http://www.ipac.caltech.edu/2mass/releases/allsky/doc/expsup.html>

Cutri R. M., Skrutskie M. F., van Dyk S., Beichman C. A., Carpenter J. M.,

- Chester T., Cambresy L., Evans T., Fowler J., Gizis J., Howard E., Huchra J., Jarrett T., Kopan E. L., Kirkpatrick J. D., Light R. M., Marsh K. A., McCallon H., Schneider S., Stiening R., Sykes M., Weinberg M., Wheaton W. A., Wheelock S., Zacarias N., 2003a, VizieR Online Data Catalog, 2246
- Di Stefano, R. & Esin A., 2012, in preparation
- Di Stefano R., 2008a, ApJ, 684, 59
- Di Stefano R., 2008b, ApJ, 684, 46
- Di Stefano R., 2009a, ArXiv:0912.1611
- Di Stefano R., 2009b, ArXiv:0912.2145
- Di Stefano R., 2011, ArXiv:1112.2366, ApJ submitted
- Di Stefano R., Esin A. A., 1995, ApJ Letters, 448, L1
- Di Stefano R., Matthews J., Lépine S., 2012a, ArXiv:1202.5316, ApJ submitted
- Di Stefano R., Matthews J., Lépine S., 2012b, ArXiv:1202.5314, ApJ submitted
- Di Stefano R., Scalzo R. A., 1999, ApJ, 512, 564
- Doyle L. R., Carter J. A., Fabrycky D. C., Slawson R. W., Howell S. B., Winn J. N., Orosz J. A., Prsa A., Welsh W. F., Quinn S. N., Latham D., Torres G., Buchhave L. A., Marcy G. W., Fortney J. J., Shporer A., Ford E. B., Lissauer J. J., Ragozzine D., Rucker M., Batalha N., Jenkins J. M., Borucki W. J., Koch D., Middour C. K., Hall J. R., McCauliff S., Fanelli M. N., Quintana E. V., Holman M. J., Caldwell D. A., Still M., Stefanik R. P., Brown W. R., Esquerdo G. A., Tang S., Furesz G., Geary J. C., Berlind P., Calkins M. L., Short D. R., Steffen J. H., Sasselov D., Dunham E. W., Cochran W. D., Boss A., Haas M. R., Buzasi D., Fischer D., 2011, Science, 333, 1602
- Dyson F. W., Eddington A. S., Davidson C., 1920, Royal Society of London Philosophical Transactions Series A, 220, 291
- Einstein A., 1911, Annalen der Physik, 340, 898
- Einstein A., 1915, Sitzungsber. preuss. Akad. Wiss. 47, 831
- Einstein A., 1916, Annalen der Physik, 354, 769
- Einstein A., 1936, Science, 84, 506
- Feibelman W. A., 1966, Science, 151, 73
- Feibelman W. A., 1986, PASP, 98, 1199
- Gaudi B. S., Bennett D. P., Udalski A., Gould A., Christie G. W., Maoz D., Dong S., McCormick J., Szymański M. K., Tristram P. J., Nikolaev S., Paczyński B., Kubiak M., Pietrzynski G., Soszyński I., Szewczyk O., Ulaczyk

K., Wyrzykowski Ł., OGLE Collaboration, DePoy D. L., Han C., Kaspi S., Lee C.-U., Mallia F., Natusch T., Pogge R. W., Park B.-G., μ -Fun Collaboration, Abe F., Bond I. A., Botzler C. S., Fukui A., Hearnshaw J. B., Itow Y., Kamiya K., Korpela A. V., Kilmartin P. M., Lin W., Masuda K., Matsubara Y., Motomura M., Muraki Y., Nakamura S., Okumura T., Ohnishi K., Rattenbury N. J., Sako T., Saito T., Sato S., Skuljan L., Sullivan D. J., Sumi T., Sweatman W. L., Yock P. C. M., MOA Collaboration, Albrow M. D., Allan A., Beaulieu J.-P., Burgdorf M. J., Cook K. H., Coutures C., Dominik M., Dieters S., Fouqué P., Greenhill J., Horne K., Steele I., Tsapras Y., Planet Collaboration, Robonet Collaborations, Chaboyer B., Crocker A., Frank S., Macintosh B., 2008, *Science* 319, 927

Gould A., Loeb A., 1992, *ApJ*, 396, 104

Griest K., Safizadeh N., 1998, *ApJ*, 500, 37

Hamilton D. P., Burns J. A., 1992, *Icarus* 96, 43

Harris H. C., Munn J. A., Kilic M., Liebert J., Williams K. A., von Hippel T., Levine S. E., Monet D. G., Eisenstein D. J., Kleinman S. J., Metcalfe T. S., Nitta A., Winget D. E., Brinkmann J., Fukugita M., Knapp G. R., Lupton R. H., Smith J. A., Schneider D. P., 2006, *AJ*, 131, 571

Hilton E. J., West A. A., Hawley S. L., Kowalski A. F., 2010, *AJ*, 140, 1402

Irwin J., Charbonneau D., Nutzman P., Falco E., 2009, in *IAU Symposium*, Vol. 253 of *IAU Symposium*, p. 37

Kaiser N., Aussel H., Burke B. E., Boesgaard H., Chambers K., Chun M. R., Heasley J. N., Hodapp K.-W., Hunt B., Jedicke R., Jewitt D., Kudritzki R., Luppino G. A., Maberry M., Magnier E., Monet D. G., Onaka P. M., Pickles A. J., Rhoads P. H. H., Simon T., Szalay A., Szapudi I., Tholen D. J., Tonry J. L., Waterson M., Wick J., 2002, Vol. 4836 of *Society of Photo-Optical Instrumentation Engineers (SPIE) Conference Series*, p. 154

Kalas P., Graham J. R., Chiang E., Fitzgerald M. P., Clampin M., Kite E. S., Stapelfeldt K., Marois C., Krist J., 2008, *Science* 322, 1345

Koch D. G., Borucki W. J., Basri G., Batalha N. M., Brown T. M., Caldwell D., Christensen-Dalsgaard J., Cochran W. D., DeVore E., Dunham E. W., Gautier, III T. N., Geary J. C., Gilliland R. L., Gould A., Jenkins J., Kondo Y., Latham D. W., Lissauer J. J., Marcy G., Monet D., Sasselov D., Boss A., Brownlee D., Caldwell J., Dupree A. K., Howell S. B., Kjeldsen H., Meibom S., Morrison D., Owen T., Reitsema H., Tarter J., Bryson S. T., Dotson J. L., Gazis P., Haas M. R., Kolodziejczak J., Rowe J. F., Van Cleve J. E., Allen C., Chandrasekaran H., Clarke B. D., Li J., Quintana E. V., Tenenbaum P.,

- Twicken J. D., Wu H., 2010, ApJ Letters, 713, L79
- Laycock S., Tang S., Grindlay J., Los E., Simcoe R., Mink D., 2008, ArXiv:0811.2005
- Lazorenko P. F., Sahlmann J., Ségransan D., Figueira P., Lovis C., Martin E., Mayor M., Pepe F., Queloz D., Rodler F., Santos N., Udry S., 2011, A&A,, 527, A25
- Lépine S., 2005, AJ, 130, 1247
- Lépine S., 2008, AJ, 135, 2177
- Lépine S., DiStefano R., 2012, ApJ Letters, 749, L6
- Lépine S., Shara M. M., 2005a, AJ 129, 1483
- Lépine S., Shara M. M., 2005b, VizieR Online Data Catalog, 1298
- Lépine S., Shara M. M., Rich R. M., 2002, AJ, 124, 1190
- Lépine S., Shara M. M., Rich R. M., 2003, AJ, 126, 921
- Mao S., Paczynski B., 1991, ApJ Letters, 374, L37
- Mayor M., Bonfils X., Forveille T., Delfosse X., Udry S., Bertaux J.-L., Beust H., Bouchy F., Lovis C., Pepe F., Perrier C., Queloz D., Santos N. C., 2009, A&A, 507, 487
- Mayor M., Queloz D., 1995, Nature, 378, 355
- Miller-Ricci E., Fortney J. J., 2010, ApJ Letters, 716, L74
- Monet D. G., Levine S. E., Canzian B., Ables H. D., Bird A. R., Dahn C. C., Guetter H. H., Harris H. C., Henden A. A., Leggett S. K., Levison H. F., Luginbuhl C. B., Martini J., Monet A. K. B., Munn J. A., Pier J. R., Rhodes A. R., Riepe B., Sell S., Stone R. C., Vrba F. J., Walker R. L., Westerhout G., Brucato R. J., Reid I. N., Schoening W., Hartley M., Read M. A., Tritton S. B., 2003, AJ, 125, 984
- Penny M. T., Kerins E., Mao S., 2011a, MNRAS, 417, 2216
- Penny M. T., Mao S., Kerins E., 2011b, MNRAS, 412, 607
- Pravdo S. H., Shaklan S. B., 2009, ApJ, 700, 623
- Richer H. B., Anderson J., Brewer J., Davis S., Fahlman G. G., Hansen B. M. S., Hurley J., Kalirai J. S., King I. R., Reitzel D., Rich R. M., Shara M. M., Stetson P. B., 2006, Science, 313, 936
- Salim S., Gould A., 2000, ApJ, 539, 241
- Schneider P., Weiss A., 1986, A&A,, 164, 237

Sion E. M., Holberg J. B., Oswalt T. D., McCook G. P., Wasatonic R., 2009,
AJ, 138, 1681

Sumi T., Bennett D. P., Bond I. A., Udalski A., Batista V., Dominik M., Fouqué P., Kubas D., Gould A., Macintosh B., Cook K., Dong S., Skuljan L., Cassan A., Abe F., Botzler C. S., Fukui A., Furusawa K., Hearnshaw J. B., Itow Y., Kamiya K., Kilmartin P. M., Korpela A., Lin W., Ling C. H., Masuda K., Matsubara Y., Miyake N., Muraki Y., Nagaya M., Nagayama T., Ohnishi K., Okumura T., Perrott Y. C., Rattenbury N., Saito T., Sako T., Sullivan D. J., Sweatman W. L., Tristram P. J., Yock P. C. M., The MOA Collaboration, Beaulieu J. P., Cole A., Coutures C., Duran M. F., Greenhill J., Jablonski F., Marboeuf U., Martioli E., Pedretti E., Pejcha O., Rojo P., Albrow M. D., Brilant S., Bode M., Bramich D. M., Burgdorf M. J., Caldwell J. A. R., Calitz H., Corrales E., Dieters S., Dominis Prester D., Donatowicz J., Hill K., Hoffman M., Horne K., Jørgensen U. G., Kains N., Kane S., Marquette J. B., Martin R., Meintjes P., Menzies J., Pollard K. R., Sahu K. C., Snodgrass C., Steele I., Street R., Tsapras Y., Wambsganss J., Williams A., Zub M., The PLANET Collaboration, Szymański M. K., Kubiak M., Pietrzyński G., Soszyński I., Szewczyk O., Wyrzykowski Ł., Ulaczyk K., The OGLE Collaboration, Allen W., Christie G. W., DePoy D. L., Gaudi B. S., Han C., Janczak J., Lee C.-U., McCormick J., Mallia F., Monard B., Natusch T., Park B.-G., Pogge R. W., Santallo R., The μ FUN Collaboration, 2010, ApJ, 710, 1641

Tang S., Grindlay J., Los E., Servillat M., 2011, in American Astronomical Society Meeting Abstracts No.217, Vol. 43 of *Bulletin of the American Astronomical Society*, No.201.07

Van Biesbroeck G., 1944, AJ, 51, 61

Wang S., Zhou J.-L., 2011, Research, Science and Technology of Brown Dwarfs and Exoplanets: Proceedings of an International Conference held in Shanghai on Occasion of a Total Eclipse of the Sun, Shanghai, China, Edited by E.L. Martin; J. Ge; W. Lin; EPJ Web of Conferences, Volume 16, id.05005 16, 5005

West A. A., Hawley S. L., Bochanski J. J., Covey K. R., Reid I. N., Dhital S., Hilton E. J., Masuda M., 2008, AJ, 135, 785

Witt H. J., 1990, A&A, 236, 311

Wolszczan A., 1994, Science 264, 538

Wolszczan A., Frail D. A., 1992, Nature, 355, 145

Appendix A

VB 10 Simulation Code

Overleaf is a printout of the Binary lens fortran code used to calculate the magnification of a binary lens. The magnification function, *mag*, was originally developed by Shude Mao, and has been modified further for the work on VB 10. This code forms only part of the programs used for the simulations during the project. The rest of the simulation work involves a combination of simple celestial mechanics simulations, combined with Monte Carlo simulations and KDTree routines to select sources from catalogues. The computational procedure is detailed in §3.

It should be noted that the indentation in this printout is inconsistent due to space considerations, but a full FORTRAN file excluding the functions and subroutines can be found at http://www.cfa.harvard.edu/plan_it/code.f.

```

Implicit none
Integer iphase,ialpha, iarr, sample, imass, val0001, peak0001, caust
c these are the arrays of integers
Integer t_pre(7), t_post(7), up(7), down(7), counter_peak,
Integer counter_vall, magup(7), magdown(7), caust1
Real*8 m1,m2,mtot,q,teta_e,teta_e_plan,a,alpha,a1,a2, G, c, msun, amp
Real*8 x1,y1,x2,y2,phi,delta,u1,u2,pi,mag,p_orb,omega,t_max, n_mj, uu
Real*8 alpha_max,alpha_min,p_max,p_min,phi_0,mag_max,phi_mag_max
Real*8 refs(7), trefs(7)
Integer i,ia,path,ip,im,it,nrnew,nday_by_2,n_dev,n_dat,idum,nstart
Parameter(nday_by_2=362,n_dev=5,pi=3.14159d0,n_dat=22251, G=6.67d-11)
Parameter(c=299792458.0d0, msun=1.98892d30)
Real*8 a_max(nday_by_2,n_dev),a_min(nday_by_2,n_dev),u(n_dat)
Real*8 mag_pt(n_dat),mag_pt1,mag_pt2,mag_bin, dev1, dev2, dev_bin
Real*8 phi_max(nday_by_2,n_dev),phi_min(nday_by_2,n_dev)
Real*8 days(n_dat),yrs, xdat, ydat,xpos(n_dat),ypos(n_dat),
      * years(n_dat)
Real*8 x_cm(n_dat),y_cm(n_dat),day_by_day(nday_by_2),
      * udis(nday_by_2),dif_in_u2,slope,mag_2,mag_1
Real*8 mag_dif,mag_dif_max,t_dif,phi_dif_mag_max, ref_now, ref_prev
Real*8 t_late, t_early
      Real*8 magpt_max, t_pt_max, deviation, dev_ref, dev_abs, tdev
      Real ran1,xx
Character(10) pathlabel
c-----
write(*,*) 'Which path would you like to study?'
read(*,*) pathlabel
c loop over 5 planet masses
Do 800 imass=1,5
  if (imass.eq.2) n_mj=3.0
  if (imass.eq.1) n_mj=1.0
  if (imass.eq.3) n_mj=0.299
  if (imass.eq.4) n_mj=0.054
  if (imass.eq.5) n_mj=0.0157
c open files according to pathlabel
Open(32,file='lc_new_3j_ '//pathlabel)
Open(31,file='lc_new_j_ '//pathlabel)
Open(33,file='lc_new_s_ '//pathlabel)
Open(34,file='lc_new_n_ '//pathlabel)
Open(35,file='lc_new_se_ '//pathlabel)
Open(42,file='peaks_new_3j_ '//pathlabel)

```

```

Open(41,file='peaks_new_j_ '//pathlabel)
Open(43,file='peaks_new_s_ '//pathlabel)
Open(44,file='peaks_new_n_ '//pathlabel)
Open(45,file='peaks_new_se_ '//pathlabel)
Open(11,file='model_days_ '//pathlabel)
c-----
c      INITIALIZE THE RANDOM NUMBER GENERATOR
      idum = -1
      do i=37595, 75181
         xx = ran1(idum)
      enddo
c-----
c sample is the sample rate in hours.
sample=2
teta_e=10.d0
magpt_max=0.0
c create reference arrays and explicitly set other to 0.
Do 107 iarr=1,7
   refs(iarr)=0.01*(2.5119**real(iarr))
   trefs(iarr)=2**real(iarr)
   up(iarr)=0
   down(iarr)=0
   t_pre(iarr)=0
   t_post(iarr)=0
   magup(iarr)=0
   magdown(iarr)=0
107 enddo
c create arrays of positions for path file
   Do 100 it=1,n_dat
      read(11,*) yrs, xdat, ydat
      xpos(it)=-xdat/teta_e
      ypos(it)=ydat/teta_e
      x_cm(it)=xpos(it)
      y_cm(it)=ypos(it)
      years(it)=yrs-2011.91718d0
      days(it)=(years(it))*365.25d0
c   We measure time in days.
c   t=0 is Dec 1, 2011 (at what time?)
      u(it)=dsqrt(xpos(it)**2+ypos(it)**2)
      uu=u(it)
      mag_pt(it)=(uu**2+2.d0)/(uu*sqrt(uu**2+4.d0))

```

```

if (mag_pt(it).gt.magpt_max) then
    magpt_max=mag_pt(it)
    t_pt_max=days(it)
endif
100 End Do
c The paths we are currently using are sampled every 0.48 hours.
m2=0.075
c note use of 0.075 mass. m2 is star, m1 is planet.
c write to the file without the planet specified.
m1=n_mj*(9.546d-4)
mtot=m1+m2
c-----
c loop over alpha
Do 202 ialpha=1,50000
c   we choose alpha randomly in log space, between 0.05, 20
    alpha=10.0d0**(-1.301d0+(2.602d0*ran1(idum)))
c   at 5.82 pc, 10 mas is 0.0582 au
c   we take the separation in au to be a= alpha*0.0582
    a=alpha*0.0582d0
    a1=alpha*m2/mtot
        a2=alpha*m1/mtot
    p_orb=365.25d0*dsqrt(a**3/mtot)
        omega=2.0d0*pi/p_orb
c   p_orb is in days, omega is in radians per day.
c   cycle over phases
Do 201 iphase=1,1
    phi_0=2.0d0*pi*ran1(idum)
    mag_max=0.0d0
    t_max=0.0d0
    phi_mag_max=0.0d0
    nrnew=3
c   We express distances in terms of the Einstein angle of VB 10,
c   which we have taken to be 10 mas.
    mag_1=1.0d0
    mag_2=1.0d0
    dev1=0.0
    dev2=0.0
    mag_dif=0.0d0
    t_dif=0.0d0
    mag_dif_max=0.0d0
    phi_dif_mag_max=0.0d0

```

```

c      t_early and t_late are latest and earliest times of peaks.
c      counters count the number of peaks and valleys >0.01 deviation
t_early=1000000000.0d0
t_late=0.0d0
counter_peak=0
counter_val1=0
c      arrays of integers reset to 0
Do 108 iarr=1,7
    up(iarr)=0
    down(iarr)=0
    t_pre(iarr)=0
    t_post(iarr)=0
    magup(iarr)=0
    magdown(iarr)=0
108     enddo
caust=0
val0001=0
val0001=0
c      now do light curves
Do 200 it=sample,n_dat,sample
    caust1=0
        phi=phi_0-omega*(days(it)-1)
        x1=x_cm(it)-a1*dcos(phi)
        y1=y_cm(it)-a1*dsin(phi)
        x2=x_cm(it)+a2*dcos(phi)
        y2=y_cm(it)+a2*dsin(phi)
        u2=dsqrt(x2**2+y2**2)
        mag_bin=mag(0.0d0,0.0d0,x1,y1,x2,y2,m1/mtot,m2/mtot,nrnew)
        dev_bin=mag_bin-mag_pt(it)
c          (dev_bin is deviation from point lens)
        if (nrnew.eq.5) caust=1
        if (nrnew.eq.5) caust1=1
c-----
c          is there a peak in the deviation?
c          bins integers according to locations/mags/devs
        If(it.ge.3*sample)Then
if(dev_abs.ge.0.001)then
    If((dev1.lt.dev2).and.(dev1.lt.dev_bin)) val0001=val0001+1
    If((dev1.gt.dev2).and.(dev1.gt.dev_bin)) peak0001=peak0001+1
endif
dev1=mag_1-mag_pt(it-sample)

```

```

    dev2=mag_2-mag_pt(it-2*sample)
    dev_abs=dabs(dev1)
    if(dev_abs.ge.0.01) then
c dev1 and dev2 are the deviation
c corresponding to mag1 and mag2 as before.
c           we study dev1 and see if it is a maxima.

c is there a valley?-----
c if there is a valley with deviation >0.01b
c bin according to characteristics, and count the valley
If((dev1.lt.dev2).and.(dev1.lt.dev_bin))Then
    counter_vall=counter_vall+1
    t_dif=days(it-sample)
    phi_dif_mag_max=phi
    tdev=t_dif-t_pt_max
write(40+imass,900) -1, ialpha, alpha, p_orb, phi_0,
    *                  caust1, dev1, mag_1, t_dif, tdev
endif

c is there a peak?-----
c if there is a peak with deviation >0.01 then
c       bin according to characteristics, and count the peak
If((dev1.gt.dev2).and.(dev1.gt.dev_bin))Then
    counter_peak=counter_peak+1
    t_dif=days(it-sample)
    phi_dif_mag_max=phi
c early and late times of peak, tdev is time deviation from pt lens max
    if (days(it).gt.t_late) t_late=days(it)
    if (days(it).lt.t_early) t_early=days(it)
        tdev=t_dif-t_pt_max
write(40+imass,900) 1, ialpha, alpha, p_orb, phi_0, caust1,
    *                  dev1, mag_1, t_dif, tdev
endif
    endif
    endif
c-----
c now set mag2,1 to next ones along
c test if the maximum magnification is exceeded
    mag_2=mag_1
    mag_1=mag_bin
    If(mag_bin.gt.mag_max)then

```

```

mag_max=mag_bin
t_max=days(it)
phi_mag_max=phi
End If
u1=dsqrt(x1**2+y1**2)
u2=dsqrt(x2**2+y2**2)/dsqrt(m1/mtot)
mag_pt1=(u1**2+2.d0)/(u1*sqrt(u1**2+4.d0))
mag_pt2=(u2**2+2.d0)/(u2*sqrt(u2**2+4.d0))
c   end of one light curve:
200   End Do
    if (t_early.eq.1000000000.0) t_early=t_pt_max
    if (t_late.eq.0.0) t_late=t_pt_max
c-----
c finished looping over the light curve,
c write arrays of integers for that light curve to file.
c write all the info to a file for that sepcific planet and path.

        write(30+imass,901) alpha, p_orb, phi_0, mag_max, caust, val0001,
        * peak0001, t_early, t_late, counter_peak, counter_vall
900 format(I4, I10, F12.4, F12.3, F12.4, I4, F12.4, F12.4, F12.4, F12.4)
901 format(F12.4, F12.4, F12.4, F12.4, I4, I4, I4, F12.4, F12.4, I4, I4)

c-----
c end of looping over phase for a given alpha:
201   End Do
c end of looping over alpha:
202 End Do
c end of looping over planet masses, close path file...
close(11)
close(30+imass)
close(40+imass)
800 enddo
End

```

Appendix B

Wide-Orbit Planets

Consider a lens star, mass M_* , with a hypothetical wide-orbit planet, separation a , mass m_p approaching a background star, with an angular distance of closest approach, b . We define two important quantities

$$\alpha = \frac{a}{R_E}; \alpha = \frac{b}{\theta_E} \quad (2.1)$$

where R_E is the Einstein radius of the lens star and θ_E is the Einstein angle of the lens star. The isomagnification contours around the planet are perturbed, and the radial size of the region of a given magnification around the planet is given by $\rho_{mag}(\delta)$, where δ is the magnification contour we are considering (i.e. the deviation required for an event to be detectable). We consider a lens approaching a source on the sky with relative proper motion of μ , such that we can view the system in the rest frame of the lens centre of mass as an approaching source star, with position vector r_s , and a planet rotating around a static point at the origin.

We must define u , the distance between the source and lens centre of mass in units of R_E . The probability of a given wide-orbit planet producing an event for a given value of β is the fraction of phases that will produce an event, and has a component dependent on the spatial characteristics of the approach and orbit, $P_{spatial}$, and a component given by the orbital motion during the time at which the source pass through the possible region of deviation, P_{motion} :

$$P = P_{spatial} + P_{motion} \quad (2.2)$$

Note that P_{motion} will either increase or decrease the probability dependent on the direction of the orbit. It should also be noted at this point that we are considering circular face on orbits, and a straight line approach. $P_{spatial}$ can be derived by simple trigonometry. The relevant isomagnification contour corresponding to δ will first 'hit' the source position at $\vec{r}_s(t) = \vec{r}_s(t_1) = \vec{r}_1$, and the source will leave

this region of possible deviations $> \delta$ at $\vec{r}_s(t) = \vec{r}_s(t_2) = \vec{r}_2$. If \vec{r}_1 and \vec{r}_2 make an angle ϕ then the distance travelled in this region, x , is given by

$$x = |\vec{r}_2 - \vec{r}_1| = \sqrt{r_1^2 + r_2^2 - 2r_1 r_2 \cos \phi} \quad (2.3)$$

$$\Rightarrow \phi = \arccos \left(\frac{r_1^2 + r_2^2 - x^2}{2r_1 r_2} \right) \quad (2.4)$$

We have $r_1 = \alpha + \rho_{mag}$, $r_2 = \alpha - \rho_{mag}$, and $x = \sqrt{r_1^2 - \beta^2} - \sqrt{r_2^2 - \beta^2}$. Since contact with this region is possible both on the way in, and the way out of the approach then we have

$$P_{spatial} = 2 \frac{\phi}{2\pi} = \frac{1}{\pi} \arccos \left(\frac{r_1^2 + r_2^2 - x^2}{2r_1 r_2} \right) \quad (2.5)$$

Using our expressions for x we can now derive P_{motion} . The time taken for the region of deviation to be passed is given by $\Delta t = t_2 - t_1 = x/\mu$. In this time the orbit will undergo a phase shift of $\psi = t/T$ where T is the planet's orbital period. This phase shift can be either direction, a property that can be contained in the angular frequency ω_f .

$$\Rightarrow P_{motion} = \frac{\omega \Delta t}{2\pi} = \frac{\omega_f x}{2\pi \mu} \quad (2.6)$$

Therefore giving us

$$P = \frac{1}{\pi} \arccos \left(\frac{r_1^2 + r_2^2 - x^2}{2r_1 r_2} \right) + \frac{\omega_f x}{2\pi \mu} \quad (2.7)$$

$$P(\alpha, \beta, \omega, \mu) = \frac{1}{\pi} \arccos \left(\frac{2\alpha^2 + 2\rho_{mag}^2 - x^2}{2\alpha^2 - 2\rho_{mag}^2} \right) + \frac{\omega x}{2\pi \mu} \quad (2.8)$$

where $x = \sqrt{(\alpha + \rho_{mag})^2 - \beta^2} - \sqrt{(\alpha - \rho_{mag})^2 - \beta^2}$.

If we consider an edge on orbit, where $i = \pi/2$ and Ω is varied then we can derive an expression for P which is valid when the condition $\alpha \geq \beta \cos \Omega - \rho_{mag}/2$ is satisfied. the area of deviation around the planet will look the same on the sky as in the face-on case, but the range of possible phases is different. We consider the region of deviation as the height h of a circular segment whose chord makes an angle θ_{ch} with the centre of the circular orbit (radius R):

$$\theta_{ch} = 2 \arccos \left(\frac{R - h}{R} \right) \quad (2.9)$$

The angle made by the range of possible orbits that could produce the deviation required (excluding the orbital motion term) is thus given by

$$\theta = 2 \arccos \left(\frac{\alpha - \rho_{mag}}{r_1 r_2} \right) \quad (2.10)$$

Substituting in $r_1 = \alpha + \rho_{mag}$, $r_2 = \alpha - \rho_{mag}$ and including the orbital motion term thus gives

$$P(\alpha, \beta, \omega_f, \mu) \approx \frac{1}{\pi} \arccos \left(\frac{\alpha + \rho_{mag}}{\alpha - \rho_{mag}} \right) + \frac{\omega_f x}{2\pi\mu} \quad (2.11)$$

As shown in §3.4.1.

Appendix C

Catalogue of VB 10 Simulation Results for Selected Approaches

The following plots, from which figure 3.8 is an example, show the results of the simulations conducted for the VB 10 event. Results are included for $b = 5, 10, 20, 50$ mas ($\beta = 0.5, 1, 2, 5$), for the 5 planet masses described previously. The counter-clockwise orbits are excluded for brevity, but give very similar forms, and because the effect of the direction motion on wide orbit planet probabilities has been discussed in appendix B.

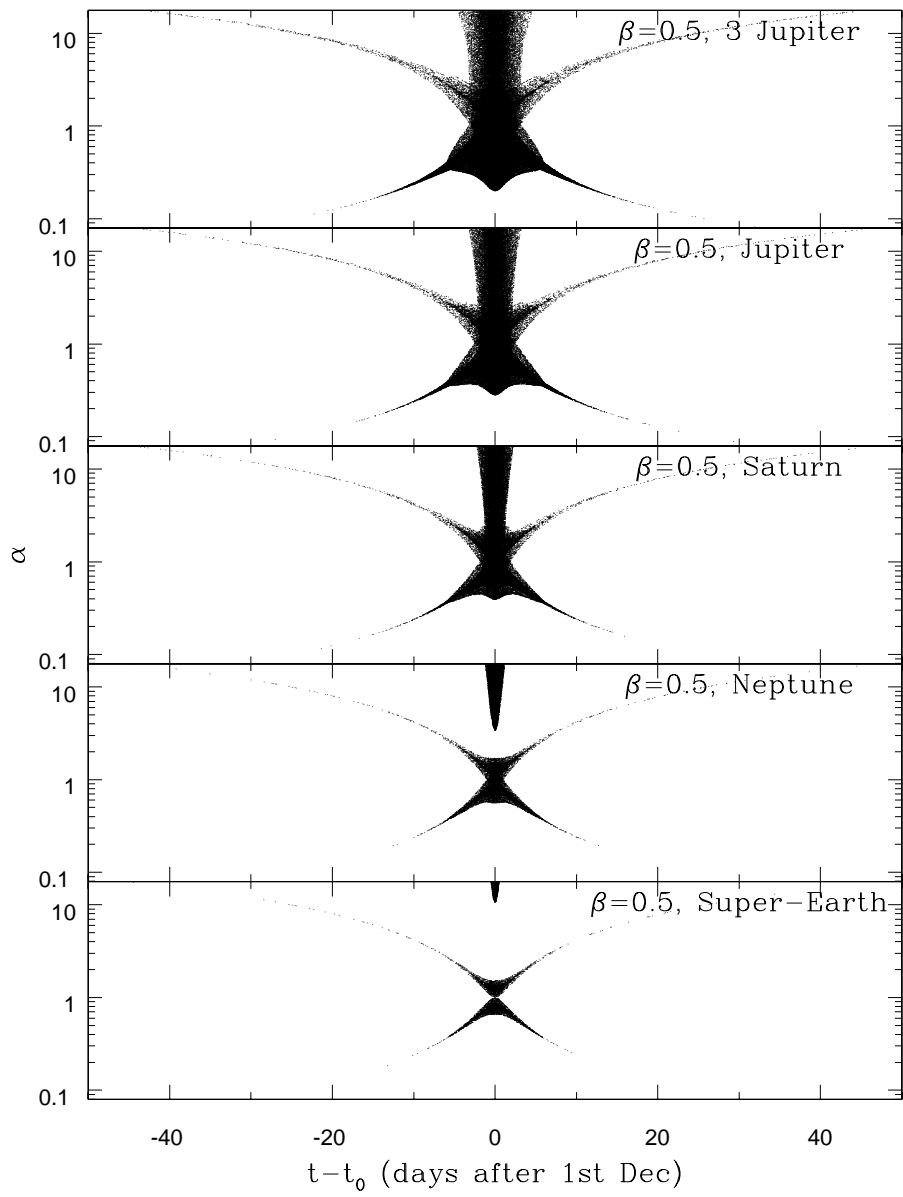


Figure C.1: Clockwise, $\beta = 0.5$, 5 different planet masses.

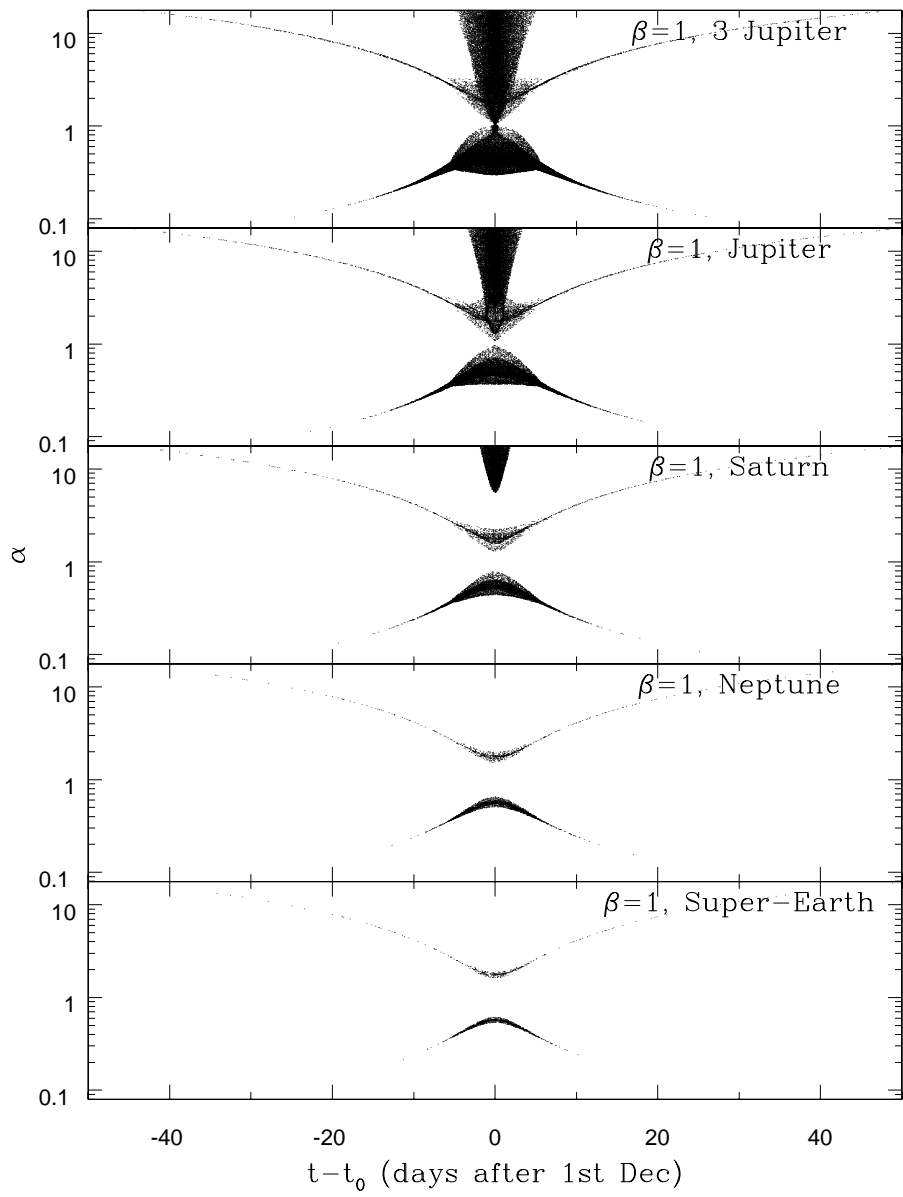


Figure C.2: Clockwise, $\beta = 1, 5$ different planet masses.

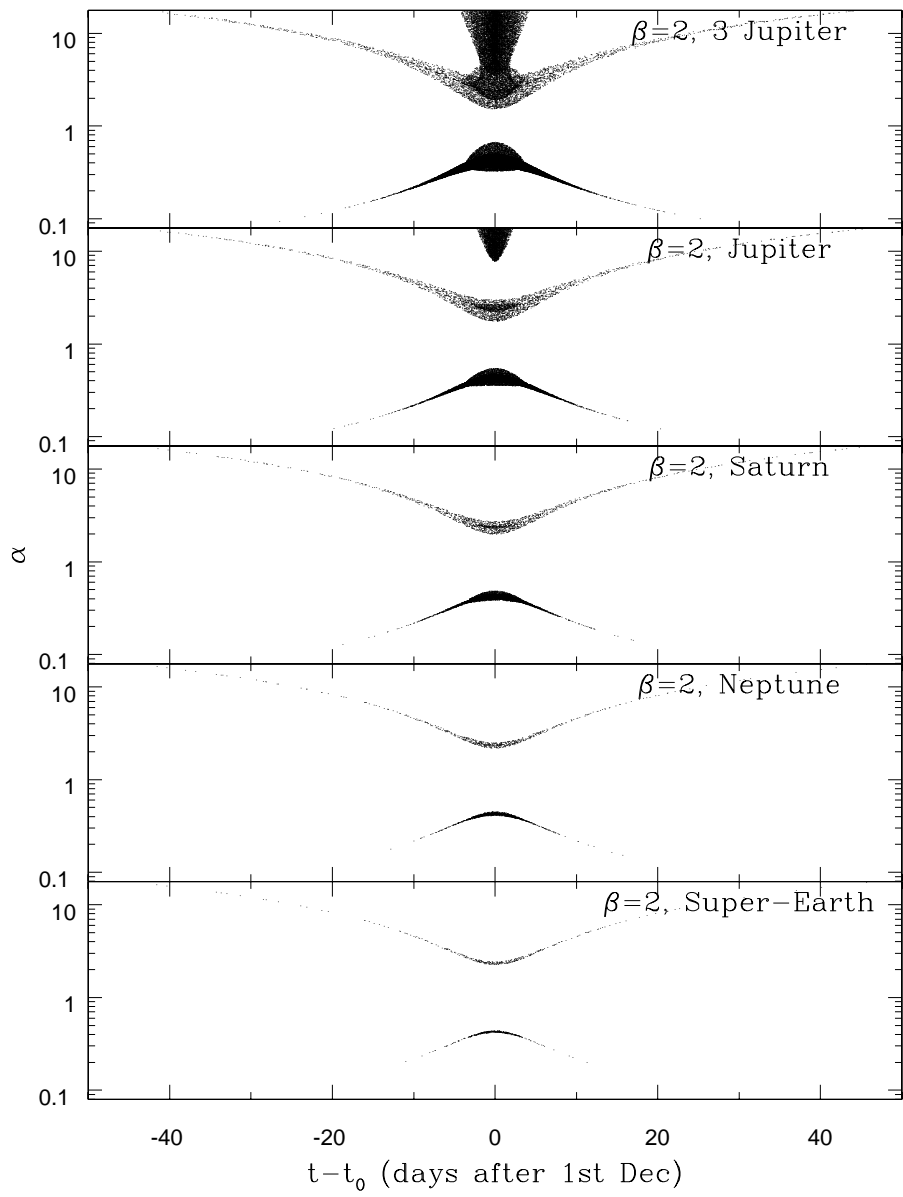


Figure C.3: Clockwise, $\beta = 2$, 5 different planet masses.

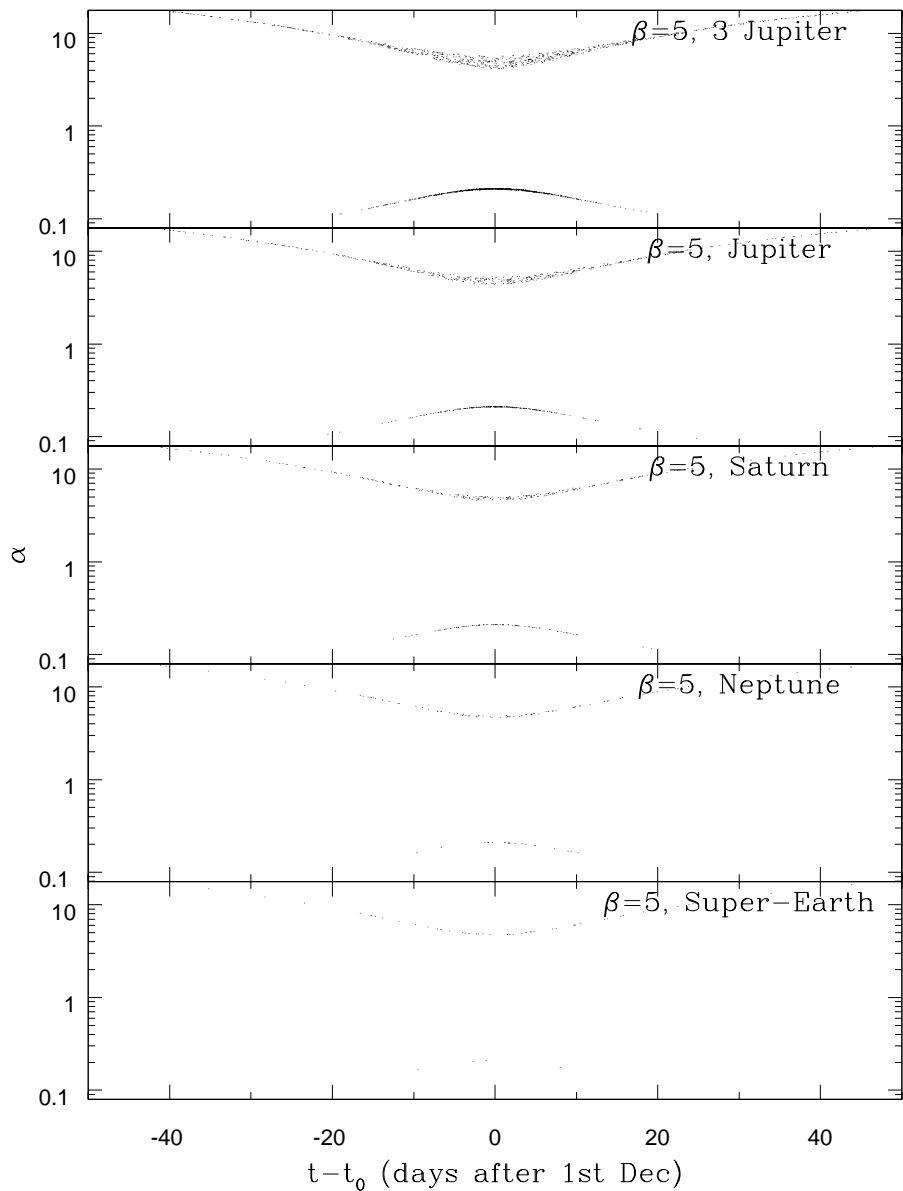


Figure C.4: Clockwise, $\beta = 5$, 5 different planet masses.

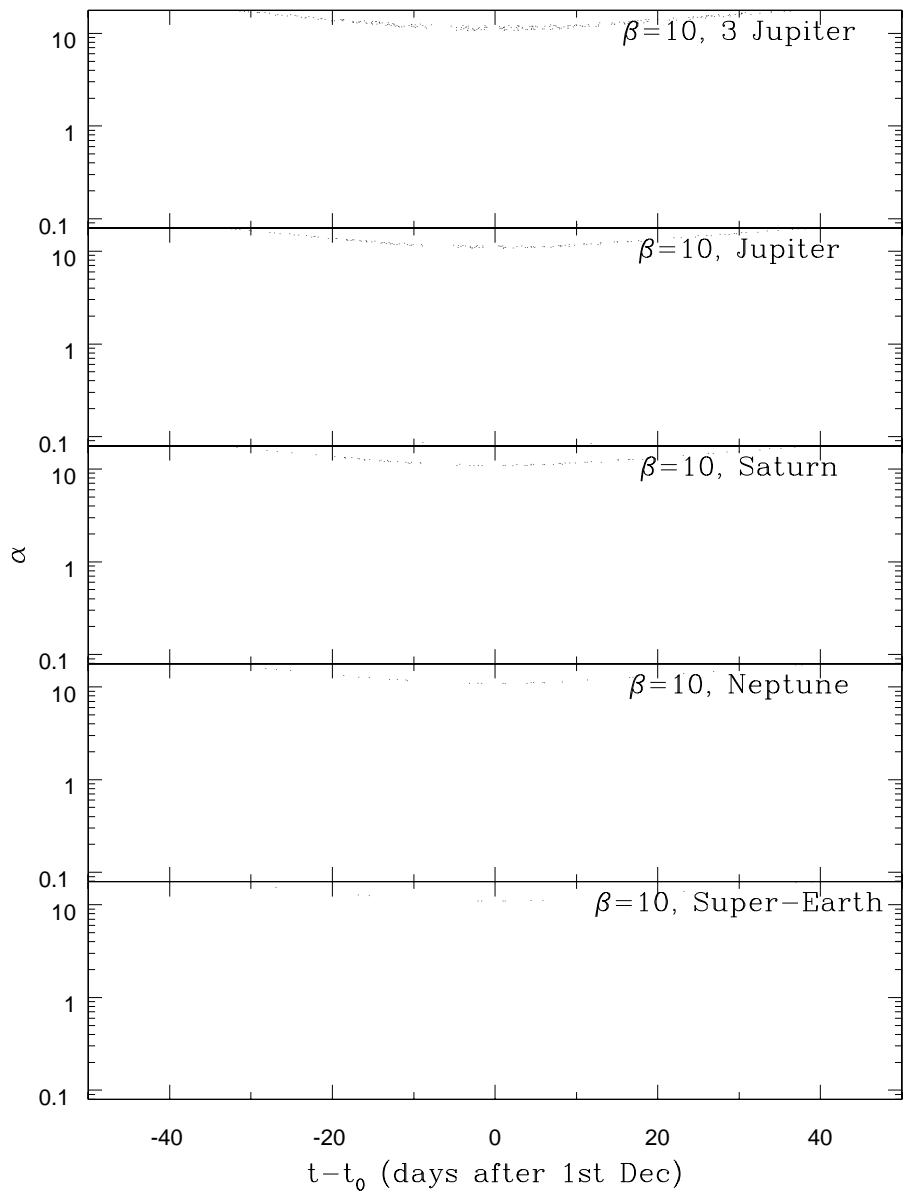


Figure C.5: Clockwise, $\beta = 10$, 5 different planet masses.

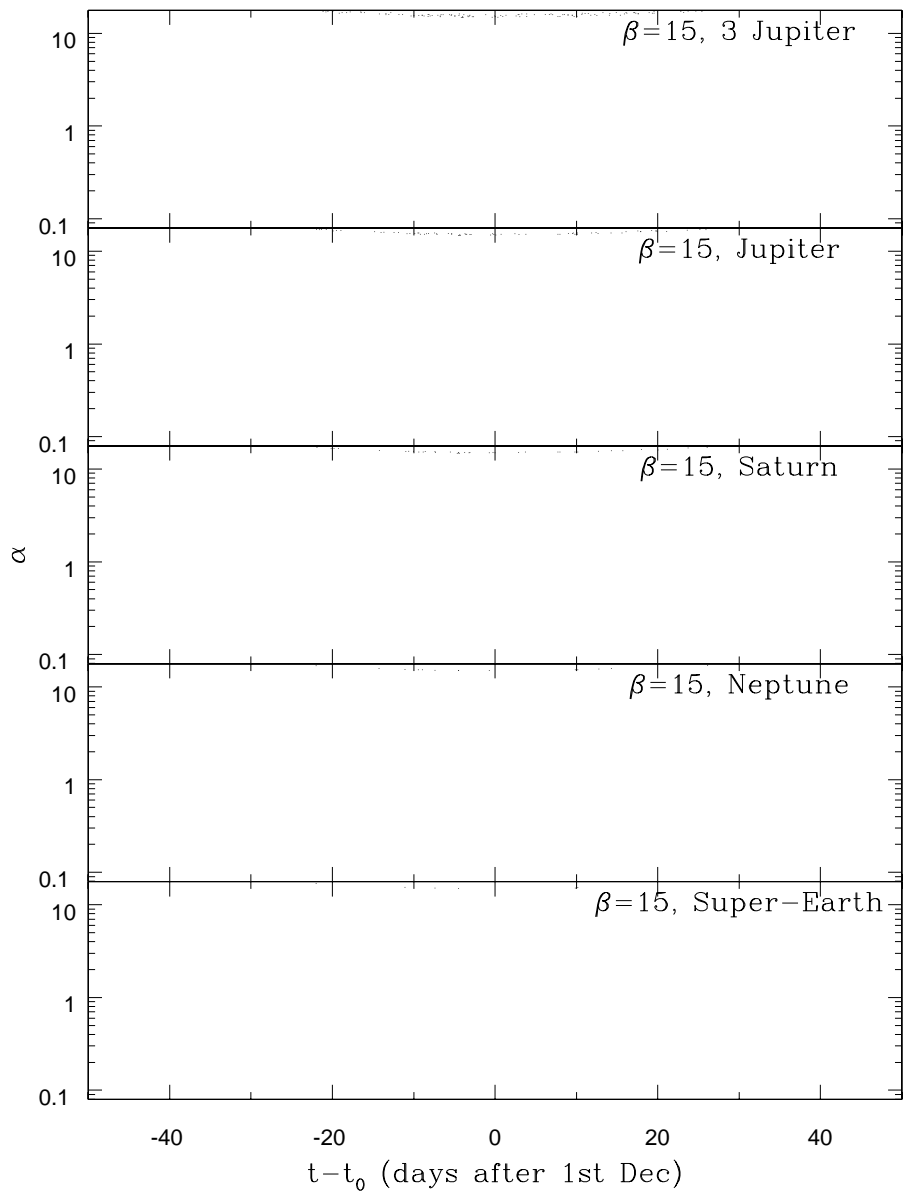


Figure C.6: Clockwise, $\beta = 15$, 5 different planet masses.